



Stellar Evolution in AGN Disks

Matteo Cantiello^{1,2} , Adam S. Jermyn¹ , and Douglas N. C. Lin^{3,4} ¹ Center for Computational Astrophysics, Flatiron Institute, 162 5th Avenue, New York, NY 10010, USA; mcantiello@flatironinstitute.org² Department of Astrophysical Sciences, Princeton University, Princeton, NJ 08544, USA³ Astronomy and Astrophysics Department, University of California, Santa Cruz, CA 95064, USA⁴ Institute for Advanced Studies, Tsinghua University, Beijing, 100086, People's Republic of China

Received 2020 September 8; revised 2021 January 13; accepted 2021 January 17; published 2021 March 30

Abstract

Active galactic nuclei (AGNs) are powered by geometrically thin accretion disks surrounding a central supermassive black hole. Here we explore the evolution of stars embedded in these extreme astrophysical environments (AGN stars). Because AGN disks are much hotter and denser than most components of the interstellar medium, AGN stars are subject to very different boundary conditions than normal stars. They are also strongly affected by both mass accretion, which can run away given the vast mass of the disk, and mass loss due to super-Eddington winds. Moreover, chemical mixing plays a critical role in the evolution of these stars by allowing fresh hydrogen accreted from the disk to mix into their cores. We find that, depending on the local AGN density and sound speed and the duration of the AGN phase, AGN stars can rapidly become very massive ($M > 100 M_{\odot}$). These stars undergo core collapse, leave behind compact remnants, and contribute to polluting the disk with heavy elements. We show that the evolution of AGN stars can have a profound impact on the evolution of AGN metallicities, as well as the production of gravitational wave sources observed by LIGO-Virgo. We point to our Galactic Center as a region well suited to testing some of our predictions for this exotic stellar evolutionary channel.

Unified Astronomy Thesaurus concepts: [Stellar evolution \(1599\)](#); [Active galactic nuclei \(16\)](#); [Stellar physics \(1621\)](#); [Massive stars \(732\)](#); [Compact objects \(288\)](#); [Gravitational waves \(678\)](#); [Stellar mass black holes \(1611\)](#); [Chemical enrichment \(225\)](#); [Galaxy chemical evolution \(580\)](#); [Bondi accretion \(174\)](#); [Stellar mass loss \(1613\)](#); [Galactic center \(565\)](#)

1. Introduction

The discovery of quasars (Schmidt 1963) led to a fundamental breakthrough in our perception of the emergence and evolution of galaxies. These powerful, sustained cosmic beacons are the brightest members of a large population of active galactic nuclei (AGNs; Ho 2008). It is widely accepted that they are powered by the release of gravitational energy as mass falls onto supermassive black holes via accretion disks at ferocious rates \dot{M}_{bh} (Lynden-Bell 1969).

Over the past five decades, observations have accumulated a vast amount of data on AGNs. In many cases, AGNs outshine their host galaxies over a wide wavelength range from radio and infrared to ultraviolet and X-ray (Elvis et al. 1994). Outflowing jets are commonly found to originate from AGNs. Depending on the relative prominence of some observed features, AGNs have been classified into subcategories. In an attempt to characterize their common phenomenological traits and exotic diversity, an empirical unified model has been proposed (Antonucci 1993; Netzer 2015) for the entire AGN population in terms of the line-of-sight prospect. In this model, AGNs possess central supermassive black holes (SMBHs, with mass $M_{\text{bh}} \sim 10^6\text{--}10^9 M_{\odot}$) that are surrounded by geometrically thin accretion disks (with aspect ratio $h = H/R \lesssim 10^{-2}$ where R and H are the disk's radius and scale height), as suggested by Lynden-Bell (1969). Farther out, at a distance of light weeks to months from the SMBH, these disks are shrouded by

geometrically thicker layers of fast-moving clouds that produce the broad emission lines seen in some AGN spectra. A well-puffed-up torus (with $h \gtrsim 10^{-1}$) of cold molecular gas is located between ≈ 0.1 and 10 pc (Nenkova et al. 2008). Since it is optically thick in the direction of the central SMBH, this torus blocks both the thin accretion disk and the broad-line regions from view if they are seen edge-on. The so-called “narrow-line region” is found farther out at $\gtrsim 10^2$ pc in the host galaxies. Compared to the broad-line region, these narrow lines are emitted by relatively small, low-density gas clouds moving at much smaller velocities (Boroson & Green 1992; Antonucci 1993; Ferrarese & Ford 2005; Ho 2008; Alexander 2017).

In the last two decades, surveys with X-Ray Multi-Mirror Mission, Sloan Digital Sky Survey, and Chandra have greatly expanded the database of AGNs and provided evidence that SMBHs coevolve with their host galaxies (Fabian 2012; Kormendy & Ho 2013; Heckman & Best 2014). The redshift-dependent AGN luminosity (L) function has been used to construct population synthesis models (Yu & Tremaine 2002; Marconi et al. 2004) to infer the energy-dissipation efficiency factor ($\epsilon = L/\dot{M}_{\text{bh}} c^2$), the ratio $\lambda = L/L_{\text{Edd}}$ where $L_{\text{Edd}} \approx 3.2 \times 10^4 L_{\odot} (M_{\text{bh}}/M_{\odot})$ is the electron-scattering Eddington limit (Equation (15)), and the duty cycles of AGNs as functions of the SMBHs' mass (M_{bh}) and redshift (z). These analyses show that the most luminous AGN phases generally last $\sim 10^{8-9}$ yr, although shorter AGN lifetimes are certainly possible (King & Nixon 2015; Schawinski et al. 2015). During these phases, M_{bh} grows substantially with $\lambda \sim 0.6$ and $\epsilon \sim 0.06$ (Raimundo & Fabian 2009; Shankar et al. 2009, 2013).



Original content from this work may be used under the terms of the [Creative Commons Attribution 4.0 licence](#). Any further distribution of this work must maintain attribution to the author(s) and the title of the work, journal citation and DOI.

Detailed spectroscopic modeling of the broad emission lines (Nagao et al. 2006; Xu et al. 2018) indicates that in AGNs, the α -element abundance is (1) generally higher than the solar value, (2) an increasing function of M_{bh} , but (3) independent of redshift. The detection X-ray fluorescence 6.4 keV K-shell emission line (Tanaka et al. 1995; Yaqoob et al. 1996; Nandra et al. 1997) suggests that iron abundance close to the SMBH may also be substantial, though there are not yet any quantitative constraints. These observed properties can be explained if heavy elements are produced in accretion disks either near or outside the broad-line regions and accreted into the supermassive black holes at the center (Artymowicz et al. 1993). Indeed, observations indicate a link between AGNs and ongoing in situ starbursts (Alexander & Hickox 2012). It has been hypothesized (Ishibashi & Fabian 2012) that rapid star formation may also lead to an elevated occurrence of supernovae, an upsurge in the dust production rate, a reduction in L_{Edd} (due to an increase in the dust opacity), the clearing of outer regions of the disk, and the quenching of AGN activities.

The common existence of SMBHs in normal galaxies is inferred from the measured surface-brightness and velocity-dispersion distribution (Kormendy & Ho 2013). In contrast, the modest occurrence rate of AGN activities suggests a low duty cycle ($\sim 10^{-2}$). The centers of typical galaxies are quiescent, and most SMBHs in galactic nuclei are accreting at a slow rate with $\lambda \ll 1$.

For example, the center of the Milky Way hosts a black hole with $M_{\text{bh}} = 4 \times 10^6 M_{\odot}$ (Genzel et al. 1997, 2010; Ghez et al. 1998, 2003a, 2008; Gillessen et al. 2009; Schödel et al. 2009; Boehle et al. 2016). Within 1 pc from it, there are $\sim 10^7$ mostly mature stars (Do et al. 2009; Genzel et al. 2010). There are also $\sim 10^2$ massive OB and Wolf–Rayet (WR) stars residing within ~ 0.05 – 0.5 pc around the Sgr A* SMBH (Krabbe et al. 1995; Genzel et al. 2003; Ghez et al. 2003b; Levin & Beloborodov 2003; Alexander 2005; Paumard et al. 2006). Their estimated age is ~ 4 – 6 Myr (Ghez et al. 2003b). Since a fraction of these young and massive stars lie in one or more orbital plane (Löckmann and Baumgardt 2009), it is often assumed that they were either formed (Goodman 2003; Levin & Beloborodov 2003) or captured and rejuvenated (Artymowicz et al. 1993; Davies & Lin 2020) in a common disk around the central SMBH. Although there are stringent upper limits on the presence of gas in the vicinity of the SMBH in the Galactic Center today (Murchikova et al. 2019), the existence of a disk, once active during or after the formation of the massive stars, may be inferred from the “Fermi Bubble” above and below the Galactic plane (Su et al. 2010). Such a disk may have λ comparable to that of accretion disks around similar-mass SMBHs in AGNs. By analogy with metal-rich AGNs, the evolution of massive stars may lead to heavy-element enrichment near Sgr A*. Supersolar metallicity has indeed been detected in the spectra of some stars within 0.5 pc from the Galactic Center (Do et al. 2018).

The possibility of stars being born inside, or captured by, an AGN disk has been extensively discussed in the literature (see, e.g., Syer et al. 1991; Artymowicz et al. 1993; Collin & Zahn 1999; Levin 2003; Goodman & Tan 2004; Nayakshin & Cuadra 2005; Collin & Zahn 2008; Wang et al. 2011; Mapelli et al. 2012; Dittmann & Miller 2020). However, the problem of the evolution of stars embedded in AGN disks has not been addressed in detail. One of the assumptions behind the conventional theory of stellar evolution is that stars evolve in

tenuous, low-temperature gas, that is, the interstellar medium. This assumption sets the outer boundary conditions of the stellar evolution problem, allowing the computation of the stellar structure and its evolution on the long nuclear-burning timescale. Even in the case of binary interactions, the stellar properties are usually only modified by episodes of mass and angular momentum exchange with a stellar companion. While potentially decisive for the final outcome (Langer 2012; de Mink et al. 2014), these episodes are usually short-lived compared to the stellar lifetime. The accepted wisdom is that stars spend the majority of their lives in a cold vacuum.

In comparison with the interstellar medium (ISM), the temperatures and densities that can be found in a large volume of AGN disks are extreme (Section 2). Therefore, stars embedded in an AGN disk should be evolved while including very different boundary conditions (Section 3) from those evolving in the ISM. In particular, AGN stars should be evolved by accounting for potentially large external temperatures, densities, and accretion rates during large fractions of the stellar lifetime (Section 4). In this paper, we discuss the adjustments required to stellar evolution models (Section 5) to calculate the structure and evolution of stars embedded in AGN disks. Using typical AGN disk conditions, we show in Section 6 the results of applying these new stellar calculations to evolve models of stars embedded in different parts of an AGN disk. In Section 7 we discuss possible observational signatures of AGN star evolution. The final section of the paper summarizes and concludes this work.

2. Stars in AGN Disks

Broadly speaking, there are two ways for a star to end up in such an extreme astrophysical environment: in situ formation (Collin & Zahn 1999, 2008; Levin 2003; Goodman & Tan 2004; Wang et al. 2011; Mapelli et al. 2012) and capture (Syer et al. 1991; Artymowicz et al. 1993).

2.1. In Situ Formation

Extended AGN accretion disks are expected to become self-gravitating and unstable to fragmentation (Paczynski 1978; Kolykhalov & Syunyaev 1980; Shlosman & Begelman 1987; Goodman 2003). It has been suggested that some gravitationally unstable AGN disks are likely to produce stars, with theoretical predictions showing a preference for the formation of massive objects (Levin 2003; Goodman & Tan 2004; Dittmann & Miller 2020). If these stars are able to further accrete after formation, then they can eventually become supermassive (Goodman & Tan 2004). For this channel, it is important to note that, although gravitational instabilities strongly amplify spiral structures and lead to torque-induced angular momentum transfer, they do not necessarily induce fragmentation and produce young stars unless the cooling time of the disk is comparable to or shorter than the local dynamical timescale (Gammie 2001, but see also Hopkins & Christiansen 2013).

2.2. Capture

Stars orbiting the central regions of galaxies can interact with the disk around an SMBH. This interaction results in energy and momentum loss that, over many passages, can bring a star into a circular orbit corotating with the disk (Syer et al. 1991; Artymowicz et al. 1993). This trapping process relies on hydrodynamical drag as well as the excitation of resonant

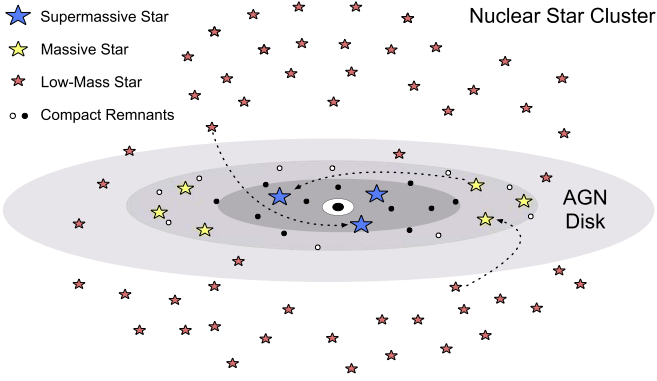


Figure 1. Schematic representation of stellar evolution in AGN disks. Stars in the inner few parsecs of the disk are the result of either capture from a nuclear star cluster or in situ formation. Their evolution is strongly affected by the local AGN conditions, and different regimes of accretion are possible (slow, intermediate, and runaway; see Section 6). In the inner regions, intermediate and runaway accretion result in a population of massive ($M > 8 M_{\odot}$) and supermassive stars ($M \gg 100 M_{\odot}$), as well as compact remnants.

density waves and bending waves, and it can be an efficient mechanism for $r \lesssim 10$ pc (Artymowicz et al. 1993; Just et al. 2012; Kennedy et al. 2016; Fabj et al. 2020; MacLeod & Lin 2020). Since the stellar density is expected to be high in these regions ($n_* \sim 10^6 \text{ pc}^{-3}$), a large number of stars can potentially be trapped during periods of AGN activity (Figure 1). The exact number depends on the AGN lifetime and the adopted AGN disk model. Panamarev et al. (2018) and Fabj et al. (2020) found that up to a few hundred stars can be captured in a megayear timescale. Assuming longer AGN lifetimes (100 Myr), Artymowicz et al. (1993) predict more than 10^4 stars could be captured by the AGN.

2.3. Observational Evidence

Direct observation of the presence of stars in AGN disks is challenging given the overpowering luminosity of the central galactic regions, especially during periods of activity (Goodman & Tan 2004). Nevertheless, in situ star formation or stellar captures could leave observational signatures in the stellar populations that are easier to observe in galactic nuclei during quiescent states. For example, compact stellar clusters are routinely found in the central ~ 5 pc of galaxies, and sometimes they coexist with SMBHs (see, e.g., Wehner & Harris 2006; Neumayer et al. 2020). In the center of our Galaxy, the young stars are observed to have a top-heavy present-day mass function (e.g., Nayakshin & Sunyaev 2005; Nayakshin et al. 2006; Paumard et al. 2006; Alexander et al. 2007; Bartko et al. 2010), which provides some evidence for stellar capture (Artymowicz et al. 1993), star formation (Levin 2003; Goodman & Tan 2004), and the findings in this paper (Section 6). Another interesting finding is the rarity of mature red-giant-branch stars and the overabundance of young, early-type stars near the Sgr A* (Buchholz et al. 2009; Do et al. 2009; Bartko et al. 2010). This correlation supports the notion that capture and rejuvenation by accretion may have enhanced the young stellar population close to galactic centers at the expense of the older population (Davies & Lin 2020), although other scenarios are possible (Davies & King 2005; Zajaček et al. 2020).

Below we first derive the typical gas conditions in AGN disks (Section 3), and then we discuss models built to calculate the evolution of stars embedded in these exotic environments (Section 4). The results of these novel calculations will give us

the ability to explore in Section 7 further observational tests for this scenario.

3. AGN Disk Model

The assessment of background density ρ and temperature T requires a model for the AGN accretion disk. In conventional accretion-disk theory (Shakura & Sunyaev 1973; Pringle 1981; Frank et al. 2002), the structure of axisymmetric, geometrically thin accretion disks is approximated through the separation of radial (R) and vertical (normal to the disk plane, z) variables under the following assumptions: (1) hydrostatic equilibrium in the direction normal to the disk plane, (2) local thermal equilibrium between the heating due to viscous dissipation and radiative cooling rates at each radii, and (3) ad hoc prescriptions of effective viscosity ν . These models provide estimates for the angular momentum transfer rates, which can be used to compute the evolution of the surface density (Σ). In a steady state, the radial distribution of Σ and the (R, z) distribution of T and ρ can then be determined in terms of the accretion rate \dot{M}_d onto an SMBH of mass M_{bh} .

In Appendix A, we derive a steady-state geometrically thin viscous disk model. We adopt the mean values of ϵ (~ 0.06) and λ (~ 0.6) obtained from previous population synthesis models of AGNs (Shankar et al. 2009, 2013). These models are relevant for luminous AGNs with signature flat spectral energy distributions (Elvis et al. 1994; Sirko & Goodman 2003). We introduce a dispersion factor f_m to include less-active AGNs, and it is equivalent to $\lambda/0.6$. Based on this model, we obtain scaling laws and estimate ranges of midplane densities (ρ_{AGN}) and sound speeds ($c_{s,\text{AGN}}$). These values provide external conditions for our AGN star models in Section 5. Bright AGNs have relatively small ($\sim 10^{-2}$) duty cycles, and most SMBHs in the centers of galaxies do not contain such a geometrically thin, opaque disk. Below some threshold \dot{M}_d (equivalently with $f_m \ll 1$), cooling becomes inefficient, and thermal instability may lead to the transformation of thin, cool disks into geometrically thick, optically thin ion tori (Ichimaru 1977; Rees et al. 1982). There is an alternative class of advection-dominated accretion-flow models that characterize gas surrounding the SMBH as both tenuous and hot (Narayan & Yi 1994). In such environments, star formation or star trapping is unlikely to occur. Moreover, accretion onto embedded stars, if any, would proceed at a negligible rate. Therefore, the analysis presented here is not applicable.

3.1. Generic Scaling Law for Marginally Self-gravitating Disks around AGNs

The gravitational stability of an accretion disk is measured in terms of

$$Q = \frac{c_{s,\text{AGN}} \Omega}{\pi G \Sigma} = \frac{h M_{\text{bh}}}{\sqrt{2} \pi \Sigma R^2} = \frac{M_{\text{bh}}}{\sqrt{8} \pi \rho_{\text{AGN}} R^3} \quad (1)$$

where $h = H/R$ is the aspect ratio, Σ is the surface density, and $\Omega (= \sqrt{GM_{\text{bh}}/R^3})$ is the Keplerian angular frequency at radius R . Regions of the disk with $Q \gtrsim 1$ are stable, and the midplane density ρ_{AGN} can be approximated with a steady-state α -viscosity prescription (see Appendix A). In the gas-pressure-dominated region, $\rho_{\text{AGN}} \propto r_{\text{pc}}^{-33/20}$ where $r_{\text{pc}} = R/1 \text{ pc}$ (Equation (A10)). For a constant opacity, $Q \propto r_{\text{pc}}^{-27/30}$ such that the outer regions of the disk are more prone to gravitational

instability (GI). Marginal stability is attained with $Q \simeq 1$ (Equations (1) and (A10)) at

$$R_Q \simeq 0.02 \left(\frac{\kappa^3 \alpha^7}{\mu^{12}} \right)^{2/27} \frac{m_8^{1/27}}{f_m^{8/27}} \text{ pc}, \quad (2)$$

where μ , κ , and α are the molecular weight, opacity, and efficiency of turbulent viscosity, and $m_8 = M_{\text{bh}}/10^8 M_\odot$ and M_\odot are the SMBH's normalized mass and the Sun's mass. A similar expression can be obtained for the radiation-pressure-dominated region.

At radius $R \gtrsim R_Q$, the conventional disk-structure models need to be modified to take into account changes in (1) the gravity normal to the disk plane (Paczynski 1978), (2) momentum transfer, and (3) possibly thermal and momentum feedback from newly formed or captured stars. In regions where marginal gravitational stability can be maintained with $Q \sim 1$, the growth of nonaxisymmetric structure leads to a torque that transports angular momentum with an equivalent $\alpha_{\text{GI}} \sim 1$ (Lin & Pringle 1987; Kratter & Lodato 2016). This efficiency is substantially larger than that resulting from MHD turbulence induced by the magnetorotational instability (MRI, $\alpha_{\text{MRI}} \sim 10^{-3}$; Bai & Stone 2011) in the inner disk region where self-gravity of the disk is negligible (with $Q \gg 1$). We adopt a convenient prescription

$$\alpha = \alpha_{\text{MRI}} f_Q + \alpha_{\text{GI}} (1 - f_Q). \quad (3)$$

We approximate the transition between GI and MRI with a dimensionless factor $f(Q)$, which steeply increases from 0 to 1 as Q increases beyond ~ 1 .

The above α - Q relationship eliminates another degree of freedom (in addition to the \dot{M}_{bh} - M_{bh} relation in Equation (A5)). It is a reasonable approximation provided Q is not much less than unity. But even with $\alpha \simeq \alpha_{\text{GI}} \sim 1$ (in Equations (A9)–(A11) and (A12)–(A14)), $Q \ll 1$ at R greater than a few R_Q . In such violently unstable disks, a global spiral structure rapidly grows and induces angular momentum transfer on a dynamical timescale (Papaloizou & Savonije 1991).

However, star formation may also be triggered in these disk regions (Gammie 2001) if their cooling timescale

$$\tau_{\text{cool}} = \frac{\mathcal{E}_{\text{th}}}{Q^-} \lesssim \frac{3}{\Omega} \quad \text{where} \quad \mathcal{E}_{\text{th}} \sim \int_{-H}^H P_{\text{rad}} dz \quad (4)$$

is the column density of thermal energy, Q^- is the thermal energy flux out of the disk (Equation (A7)), and P_{rad} is the radiation pressure. In the gas (P_{gas})/radiation-pressure-dominated regions (with $\beta_{\text{p}} \equiv P_{\text{gas}}/P_{\text{rad}} \gtrsim 1$) $\mathcal{E}_{\text{th}} \sim \Sigma R_g T_{\text{AGN}}/\mu$ and $\sim 2aT_{\text{AGN}}^4 H/3$, respectively. Both limits can be taken into account with

$$\mathcal{E}_{\text{tot}} \sim \frac{2}{3} (1 + \beta_{\text{p}}) a T_{\text{AGN}}^4 H \quad (5)$$

where T_{AGN} is the midplane temperature. The cooling time τ_{cool} , in the opaque (where the optical depth of the disk $\tau \gg 1$) limit, is

$$\tau_{\text{cool}} \simeq \frac{4(1 + \beta_{\text{p}})H\tau}{3c} = \frac{4\sqrt{2}(1 + \beta_{\text{p}})c_{s,a}\tau}{3c\Omega} \quad (6)$$

(Equation (A3)). In thermal equilibrium where the local viscous dissipation is balanced by the radiative diffusion, $\tau_{\text{cool}} \sim 1/\alpha\Omega$

(Pringle et al. 1973). In this case, the necessary condition for star formation (i.e., Equation (4)) is attainable in the limit of marginal gravitational stability ($Q \sim 1$) when $\alpha \sim 1$ (Equation (3)).

The onset of star formation leads to additional momentum and energy sources such as stellar luminosity, wind, supernovae, and accretion onto their remnants. These processes increase T_{AGN} , $c_{s,\text{AGN}}$ (the midplane sound speed), and H . They also increase Q and τ_c as well as reduce α and therefore reduce the heating rate. With a self-regulated star formation rate, marginal gravitational stability may be maintained with $Q \sim 1$ outside R_Q . Here we introduce a scaling law to construct a generic model for marginally stable disk regions at $R \gtrsim R_Q$.

From the steady-state \dot{M}_{bh} - M_{bh} relation (Equation (A5)),

$$\dot{M}_d = \dot{M}_{\text{bh}} = 3 \frac{\alpha h^3}{Q} M_{\text{bh}} \Omega \quad \text{and} \quad (7)$$

$$h = \left(\frac{\dot{M}_d Q}{3\alpha M_{\text{bh}} \Omega} \right)^{1/3} = \frac{f_m^{1/3} Q^{1/3}}{\alpha^{1/3}} h_Q, \\ h_Q \equiv \frac{0.025 r_{\text{pc}}^{1/2}}{m_8^{1/6}}, \quad (8)$$

where \dot{M}_d is the mass flux through the disk. The corresponding midplane and surface density are

$$\rho_{\text{AGN}} = \frac{\rho_Q}{Q}, \quad \rho_Q \equiv \frac{M_{\text{bh}}}{\sqrt{8} \pi R^3} \\ = 8.3 \times 10^{-16} \frac{m_8}{r_{\text{pc}}^3} \text{ g cm}^{-3}, \quad (9)$$

$$\Sigma = \frac{f_m^{1/3} \Sigma_Q}{Q^{2/3} \alpha^{1/3}}, \quad \Sigma_Q \equiv 2\rho_Q h_Q r \\ = \frac{180 m_8^{5/6}}{r_{\text{pc}}^{3/2}} \text{ g cm}^{-2}. \quad (10)$$

From the midplane sound speed,

$$c_{s,\text{AGN}} = \frac{h\Omega R}{\sqrt{2}} \sim \frac{f_m^{1/3} Q^{1/3}}{\alpha^{1/3}} c_{s,Q}, \\ c_{s,Q} \equiv 10^6 m_8^{2/3} \text{ cm s}^{-1}, \quad (11)$$

we find the midplane temperature for the gas/radiation-pressure-dominated regions:

$$T_{\text{AGN,gas}} = \left(\frac{f_m Q}{\alpha} \right)^{2/3} T_{Q,\text{gas}}, \\ T_{Q,\text{gas}} \simeq 1.3 \times 10^4 m_8^{2/3} \text{ K} \\ T_{\text{AGN,rad}} \sim \frac{f_m^{1/6} T_{Q,\text{rad}}}{\alpha^{1/6} Q^{1/12}}, \\ T_{Q,\text{rad}} \sim 1.4 \times 10^3 \frac{m_8^{5/12}}{r_{\text{pc}}^{3/4}} \text{ K}. \quad (12)$$

If marginal gravitational stability is maintained outside R_Q , the outer regions of the disk would have $Q \sim 1$ and $\alpha \sim 1$ with $h \sim h_Q$, $\rho_{\text{AGN}} \sim \rho_Q$, $c_{s,\text{AGN}} \sim c_{s,Q}$, $T_{\text{AGN,gas}} = T_{Q,\text{gas}}$, and $T_{\text{AGN,rad}} = T_{Q,\text{rad}}$. Equations (8), (9), (11), and (12) provide a

range of densities and sound speeds for the AGN disk. Note that in Equation (11), $c_{s,AGN}$ is independent of R .

3.2. Additional Heating Mechanisms

Similar to protostellar disks (Garaud & Lin 2007), irradiation on the disk surface can significantly increase the heating flux (Q^+) and the effective temperature on the disk surface (T_e) and midplane (T_{AGN}) in the outer regions of the disk. In addition, embedded stars, formed in situ or captured by the disk, provide additional heat sources. Moreover, their neutron star or black hole byproducts continue to accrete disk gas and radiate, due to the dissipation of gravitational energy. In the present investigation on the evolution of stars in AGN disks, we consider regions of ongoing star formation or star trapping with $Q \sim 1$ and $\alpha \sim \alpha_{GI} \sim 1$. For the initial exploration of a generic set of model parameters, we adopt T_{AGN} (10^{2-3} K), ρ_{AGN} (10^{-17} – 10^{-15} g cm $^{-3}$), and $c_{s,AGN}$ (3–100 km s $^{-1}$). Additional models with a more extended range of disk properties will be examined in subsequent papers. The maintenance of a thermal equilibrium in such disk regions requires “auxiliary energy sources” to the viscous dissipation in conventional disk models. Some possible contributors include nuclear fusion from embedded stars or accretion power from their remnants (Goodman 2003; Thompson et al. 2005). These sources may also significantly modify an AGN’s spectral energy distribution (Sirko & Goodman 2003). The construction of a self-consistent stellar-feedback model, including the results in this paper, will be presented elsewhere.

4. Modeling Stellar Evolution in AGN Disks

As discussed in Section 2, theoretical arguments and observations suggest that stars can find themselves inside AGN disks. In this section we discuss the physical ingredients that we implemented in our models to simulate the evolution of such objects, which we call AGN stars.

4.1. Accretion

A star of mass M_* at rest relative to gas of density ρ_{AGN} and temperature T_{AGN} inside an AGN disk accretes material at a rate

$$\dot{M}_B = \eta \pi R_B^2 \rho_{AGN} c_{s,AGN}, \quad (13)$$

where $c_{s,AGN}$ is the local sound speed in the disk, R_B is the Bondi radius defined as

$$R_B = \frac{2GM_*}{c_{s,AGN}^2}, \quad (14)$$

and η is an efficiency factor ($\eta \leq 1$).

The amount of material that is actually accreted depends on the ability of the inflow to lose angular momentum and on the radiation feedback from the accreting object. While the need to shed angular momentum can severely reduce the accretion rate onto compact objects (Li et al. 2013; Roberts et al. 2017; Inayoshi et al. 2018), the ratio $R_B/R_* \sim 10^{2-4}$ is much smaller for AGN stars than for BHs and neutron stars ($\sim 10^8$), so this is less of a barrier to accretion. We will return to discussing the radiation feedback on accretion in Section 4.3.

In our models, we use Equation (13) with an accretion efficiency $\eta = 1$. However, since $\dot{M}_B \propto \eta \rho_{AGN} / c_{s,AGN}^3$ ($\propto \eta \rho_{AGN} / T_{AGN}^{3/2}$), a different choice of η is equivalent to a rescaling of the

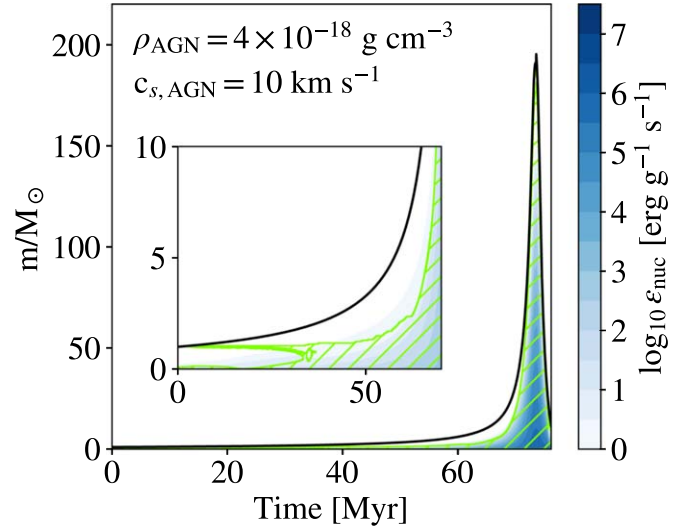


Figure 2. Evolution of total mass as a function of time for a model of an AGN star at a density of 4×10^{-18} g cm $^{-3}$ and sound speed 10 km s $^{-1}$. The green hatched regions are convective, and the blue shading shows the rate of nuclear energy generation. The inset shows a zoom-in on the first 70 Myr of evolution.

local AGN conditions. For example, for a fixed T_{AGN} , an AGN star model with $\rho_{AGN} = 10^{-16}$ g cm $^{-3}$ and $\eta = 1$ is identical to one with $\rho_{AGN} = 10^{-15}$ g cm $^{-3}$ but an accretion efficiency $\eta = 0.1$. We also assume that the star accretes material with a fixed composition ($X = 0.72$, $Y = 0.28$), and that the entropy of the accreted material is the same as that of the stellar surface. The latter assumption corresponds to an accretion process in which advection is slower than thermal equilibration. In Appendix C we demonstrate that this holds.

For the range of ρ_{AGN} , T_{AGN} , and $c_{s,AGN}$ we are considering for AGN disks, \dot{M}_B is comparable to or larger than that in star-forming, dense molecular cores.⁵ Since massive stars can emerge within 10^6 yr in the latter, we expect massive stars to rapidly grow in AGNs.

In Figure 2 we show the evolution of total mass as function of time for a model of an AGN star at a density of 4×10^{-18} g cm $^{-3}$ and sound speed 10 km s $^{-1}$ (corresponding to a radiation-dominated AGN temperature of about 186 K). Accretion initially dominates and, after about 73 Myr, the star reaches a mass of approximately $200 M_\odot$. We will discuss the subsequent evolution of this model after introducing our implementation of mass loss.

4.2. Mass Loss

The large accretion rates that can characterize the evolution of AGN stars result in very massive stars with vigorous nuclear burning. Hence, many AGN stars reach the Eddington luminosity

$$L_{\text{Edd}} \equiv \frac{4\pi GM_* c}{\kappa} = 3.2 \times 10^4 \left(\frac{M_*}{M_\odot} \right) L_\odot, \quad (15)$$

where κ is the opacity, and we used the electron-scattering value to calculate the scaling relation on the right-hand side of Equation (15). When the stellar luminosity exceeds this limit,

⁵ These have densities of order $\sim 10^{-20}$ g cm $^{-3}$ and temperatures of order ~ 10 K.

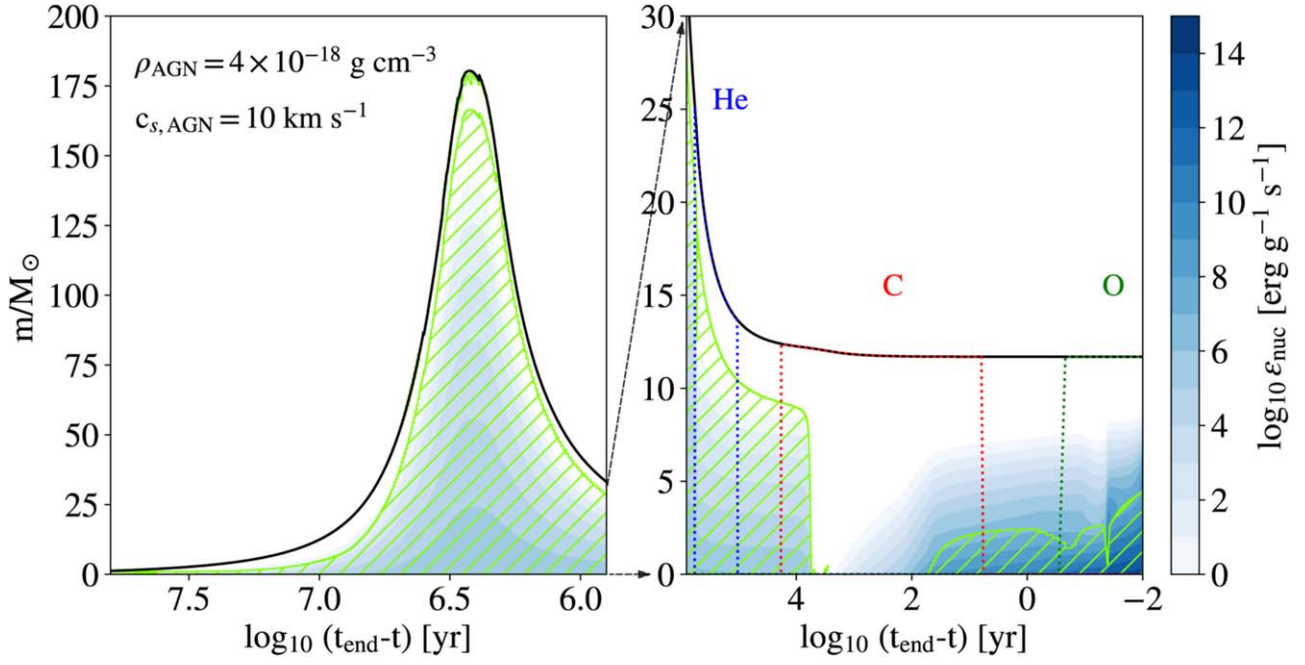


Figure 3. Same as Figure 2, but as a function of logarithm of time until the end of the calculation (oxygen burning). The right panel highlights the late stages of evolution, showing how the model composition becomes first helium-, then carbon-, and finally oxygen-rich. The calculation reached a core temperature $\log_{10} T_c / \text{K} \simeq 9.5$.

high mass-loss rates are expected (e.g., Owocki & Shaviv 2012; Smith 2014). While the details of this process are complex (Maeder & Meynet 2000; Owocki et al. 2004; Gräfener and Hamann 2008; Gräfener et al. 2011; Quataert et al. 2016; Jiang et al. 2018b), similar to other works (e.g., Paxton et al. 2011), we assume a super-Eddington outflow at the escape velocity $v_{\text{esc}} = (2GM_*/R_*)^{1/2}$, with the scale set by the excess luminosity $L_{\text{Edd}} - L_*$. In particular, we take

$$\dot{M}_{\text{Edd}} = -\frac{L_*}{v_{\text{esc}}^2} \left[1 + \tanh \left(\frac{L_* - L_{\text{Edd}}}{0.1L_{\text{Edd}}} \right) \right], \quad (16)$$

a phenomenological form where the tanh term is used to smooth the onset of mass loss and help the calculations converge. We have chosen to use v_{esc} at the stellar radius, which in our models is the shock radius (i.e., the point where the accretion stream merges with the nearly hydrostatic star). This is the relevant velocity scale because escaping material begins stationary at R_* and has to reach at least v_{esc} to escape. We further note that using the full opacity in Equation (15) leads to a lower value of the Eddington luminosity, which in turn results in larger mass-loss rates.

Because of mass accretion and helium enrichment, our model in Figure 2 approaches the Eddington luminosity after ≈ 70 Myr, which drives a super-Eddington stellar wind that eventually dominates over accretion and causes a decrease of its total mass (Figures 2–4). At the end of its evolution, the model has a mass of $\approx 10M_\odot$ (Figure 3) and is expected to undergo core collapse and leave behind a compact remnant.

As we show in Section 6, our models of massive and very massive AGN stars evolve with $L_* \simeq L_{\text{Edd}}$. As such, we expect their mass loss to be completely dominated by super-Eddington, continuum-driven winds, and therefore we do not include any

wind mass loss caused by line driving (Lamers & Cassinelli 1999; Vink et al. 2001; Vink & de Koter 2005; Smith 2014).

4.3. Interplay between Accretion and Mass Loss

When AGN stars exceed their Eddington luminosities, we expect a complex interplay between accretion and mass loss. In particular, we expect that turbulent eddies break spherical symmetry, allowing the system to form separated channels of inflows and radiation-dominated outflows.⁶ The star should then be both accreting *and* losing mass at the same time.

In our models, we include the effects of accretion and mass loss as follows. For $L_* < L_{\text{Edd}}$, we just add material to the star according to Equation (13). For $L_* \geq L_{\text{Edd}}$, we first calculate a reduced accretion rate

$$\dot{M}_{\text{B},\Gamma} = \dot{M}_{\text{B}}(1 - \tanh|L_*/L_{\text{Edd}}|), \quad (17)$$

which accounts for the decreased solid angle available to accretion as the star drives a super-Eddington outflow. This form is purely phenomenological and was chosen to be smooth and satisfy the constraints of giving the unmodified Bondi accretion rate when $L_* \ll L_{\text{Edd}}$ and zero accretion when $L_* \gg L_{\text{Edd}}$.

Ordinarily, MESA takes a time step by first changing the mass of a model and then calculating its time evolution through a time step dt at fixed mass. To incorporate the effect of simultaneous mass loss and accretion on the composition of our models, we modify this procedure so that in each step we first remove an amount of material

$$\Delta M_{\text{loss}} = \dot{M}_{\text{Edd}} dt, \quad (18)$$

⁶ In the presence of rotation, such symmetry breaking is likely promoted by the fact that rotating stars have hot poles and cool equators. In that case, one might expect polar outflows to be removing mass from the star, while reduced accretion might still occur closer to equatorial regions.

and subsequently add an amount of material

$$\Delta M_{\text{gain}} = \dot{M}_{\text{B},\Gamma} dt. \quad (19)$$

The ordering of these allows the AGN stars to release nuclear-processed material back to the AGN *even when* it is net accreting ($\dot{M}_{\text{B},\Gamma} > \dot{M}_{\text{Edd}}$); see, for example, Figure 5.

This procedure is valid so long as the surface composition of the star is uniform down to a mass depth ΔM_{loss} . As we argue in Section 4.4, whenever these models undergo super-Eddington mass loss, they should also be well mixed, so this is not a concern for our calculations.

The qualitative evolution of AGN stars close to the Eddington limit does not depend too much on the details of how material is added and removed so long as three qualitative features hold:

1. AGN stars are able to release nuclear-processed material back to the AGN.
2. AGN stars reaching the Eddington limit lose mass at an increasing rate as L_*/L_{Edd} increases.
3. Accretion onto AGN stars slows as L_*/L_{Edd} increases.

4.4. Internal Mixing

As AGN stars accrete material and become more massive, we expect them to become increasingly mixed. This occurs for several reasons. First, massive stars have large convective cores that grow as the star becomes more massive. We shall see that AGN stars also form such cores, which are well mixed by convection. Second, AGN stars become increasingly radiation dominated as they become more massive. This occurs in normal massive stars as well, but because of the unusual surface boundary conditions of stars embedded in AGNs (Section 4.5), the entire star often evolves to a state where $P_{\text{rad}} \approx P_{\text{gas}}$. This means that the star is nearly a $\gamma = 4/3$ polytrope, which radically reduces the threshold for any instability to develop, such that even radiative regions can be extensively affected by mixing processes (see, e.g., Jiang et al. 2015, 2018b).

Moreover, the interplay of accretion and mass loss is likely to drive strong circulations in the outer radiative part of the star. For example, if mass accretion occurs preferentially in the equatorial regions while mass is lost primarily in the form of polar winds, a strong meridional flow will be driven to restore pressure balance. This is the case even in the absence of rotational mixing, though rotational mixing is also likely to be important when AGN stars accrete material with significant angular momentum. We will study the impact of rotation on AGN star evolution in future works.

We model the effect of mixing by adding a compositional diffusivity D that increases with stellar luminosity as

$$D = H_p \left(\frac{F}{\rho} \right)^{1/3} \tanh \left(\frac{L_*}{L_{\text{Edd}}} \right)^\xi, \quad (20)$$

where F is the heat flux and

$$H_p \equiv \frac{P}{\rho g} \quad (21)$$

is the local pressure scale height. The form of this additional diffusivity is set to be on the order of the convective diffusivity *were the region efficiently convectively unstable*. We chose a

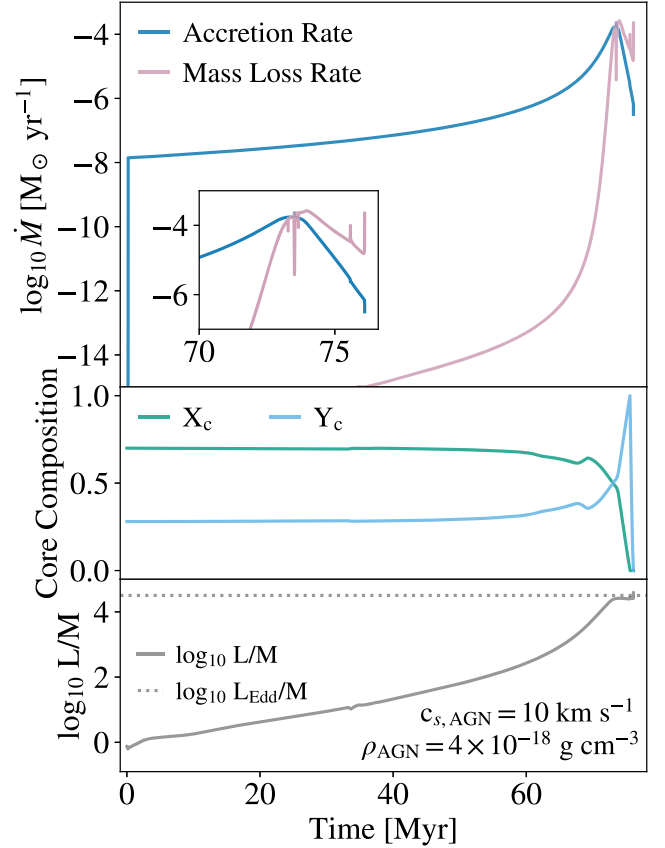


Figure 4. Time evolution of accretion and mass-loss rates in an AGN star model evolved at a density of $4 \times 10^{-18} \text{ g cm}^{-3}$ and ambient sound speed 10 km s^{-1} (top panel). The core composition is shown in the middle panel (X_c and Y_c are the core hydrogen and helium mass fractions, respectively). The ratio of stellar luminosity to mass (L/M) in solar units is shown in the bottom panel and compared to the Eddington value.

large value of the exponent ($\xi = 7$) so that stars become well mixed only when they get very close to the Eddington limit. With this prescription, AGN stars that accrete large amounts of mass and reach their Eddington luminosity do not build substantial compositional gradients while burning hydrogen in their cores, and they evolve quasi-chemically homogeneously (Maeder 1987; Yoon & Langer 2005). On the other hand, AGN stars that only accrete a few solar masses of material evolve mostly as canonical stars. We note that our results depend very weakly on the specific choice of $\xi > 1$.

We show in Figure 6 the result of this mixing implementation for our AGN star model with a density and ambient sound speed of $4 \times 10^{-18} \text{ g cm}^{-3}$ and 10 km s^{-1} , respectively. The plots show the increasing role of internal mixing as the stellar mass increases, with an increasing value of the compositional diffusivity leading to mixing of He-rich material outside of the stellar convective core and into the radiative stellar envelope starting at an age of $\approx 67 \text{ Myr}$. This mixing also leads to a partial rejuvenation of the star, with H-rich material supplied to the stellar core (see bumps in the core composition visible at $\approx 67 \text{ Myr}$ in the middle panel of Figure 4). The increased stellar mass and helium abundance in the envelope are responsible for the model reaching the Eddington luminosity. Later in the evolution, mass loss is also responsible for revealing to the surface nuclear-processed material, which in turn can have an impact on mass loss itself (by increasing the ratio of stellar

luminosity to mass). The two spikes in mass-loss rate visible in the inset of Figure 4 (top panel) correspond to the stellar surface abundances becoming helium and oxygen dominated, respectively (see right panel in Figure 3).

4.5. Surface Boundary Conditions

Accretion often involves a shock at which material slows from supersonic to subsonic. To avoid modeling the accretion shock in MESA, we place the outer boundary of the MESA model just inside the shock. To do this, we must specify the surface pressure and temperature of the model as functions of L_* , M_* , R_* , and the AGN properties.

We derive the structure of the accretion stream, and hence of the surface of the stellar model, by making the following assumptions and approximations:

1. The stream is spherically symmetric.
2. The stream is in a steady state.
3. The stream is not pressure supported.
4. The stream primarily transports heat via radiative diffusion.
5. The luminosity is constant in the stream.
6. The mass of the stream is small compared with M_* .
7. The opacity of the stream is constant in space and equal to the electron-scattering value.

In Appendix D we verify that the resulting solution either obeys these or is not significantly altered if they fail to hold.

Assumptions 3 and 7 are the most suspect. Radiation pressure may be significant when $L_* \approx L_{\text{Edd}}$, but we think that even in such cases the answer is unlikely to be very different from what we derive below. Likewise, the opacity almost certainly varies substantially throughout the accretion stream, and our neglect of this variation could introduce systematic errors into our calculations. Because the opacity only enters in setting a small part of the shock pressure and the total temperature difference between the AGN and the stellar photosphere, our hope is that using a suitable average value is not a bad approximation, but we have no proof to that effect.

4.5.1. Preshock Properties

With our assumptions, the inviscid Navier–Stokes equation reads as

$$\frac{\partial}{\partial r} \left(\frac{1}{2} v^2 \right) + \frac{GM_*}{r^2} = 0, \quad (22)$$

and mass continuity becomes

$$\dot{M} = 4\pi r^2 \rho v = \text{const.} \quad (23)$$

Assuming the material is stationary at infinity, we find

$$v \approx \sqrt{\frac{GM_*}{r}}. \quad (24)$$

Inserting this into Equation (23), we obtain

$$\rho = \frac{\dot{M}}{4\pi r^2} \sqrt{\frac{r}{GM_*}}. \quad (25)$$

The equation of radiative thermal equilibrium is

$$\frac{dT}{dr} = -\frac{3\kappa\rho L}{64\pi r^2 \sigma T^3}. \quad (26)$$

With fixed κ and L , and using $\rho \propto r^{-3/2}$, we find that at high optical depth

$$T \propto r^{-5/8}. \quad (27)$$

4.5.2. Postshock Properties

Because thermal diffusion is much faster than thermal advection over scales of R_* (see Appendix D), there is no significant temperature jump at the shock. Rather, the increased entropy is turned promptly into luminosity, of order

$$L_{\text{shock}} \sim \dot{M} v^2, \quad (28)$$

which is added to L_* to set the total luminosity in the accretion stream.

Because there is no temperature jump, the surface temperature of the star is just that of the base of the stream. To smoothly connect the limit of an optically thick accretion stream to an optically thin one, we let

$$T_{\text{eff}} \equiv \left(T_{\text{AGN}}^4 + \frac{L}{4\pi R_{\text{ph}}^2 \sigma} \right)^{1/4} \quad (29)$$

and

$$T_* = T_{\text{eff}} \left(\frac{R_*}{R_{\text{ph}}} \right)^{-5/8}, \quad (30)$$

where T_{eff} is the temperature at the photosphere, T_* is the temperature of the surface cell, and R_{ph} is the photosphere radius. To calculate this, note that the optical depth between R_B and r in the stream is

$$\tau = \int_{R_B}^r \kappa \rho dr. \quad (31)$$

Using Equation (25) and taking the opacity to be fixed, we find that, far inside R_B ,

$$\tau \approx \kappa \rho_{\text{AGN}} R_B \sqrt{\frac{R_B}{r}}. \quad (32)$$

Because we include the effects of incident radiation from the AGN in Equation (30), the photosphere occurs when the optical depth between R_B and R_{ph} is $\tau \sim 1$, giving

$$R_{\text{ph}} \sim \min(R_B, R_* + \kappa^2 \rho_{\text{AGN}}^2 R_B^3), \quad (33)$$

where we have added R_* so that when the stream is optically thin, Equation (33) gives $R_{\text{ph}} = R_*$, and this reduces to the usual Eddington atmospheric condition that places the photosphere at the edge of the stellar model. Note that we include the term T_{AGN}^4 to account for radiation incident from the AGN, along lines similar to the boundary condition of Tout et al. (1989).

To summarize, the stellar radius R_* corresponds to the outer grid point of our MESA calculation and the location of the accretion shock. The corresponding temperature is T_* . The photospheric radius R_{ph} corresponds to the radius of the star as seen from an observer located at R_B . The temperature at R_{ph} is T_{eff} . We show the evolution of the relevant radii of AGN stars for one of our models in Figure 7. Note that, depending on the properties of the surrounding AGN disk, R_{ph} and T_{eff} might not

be stellar observables. Finally, for $\dot{M}_B \rightarrow 0$, $R_{\text{ph}} \rightarrow R_*$ and $T_{\text{eff}} \rightarrow T_*$.

The pressure just after the shock is given by the sum of gas and radiation pressure. This is related to the pressure just before the shock by the ram pressure, so we write

$$P_{\text{after}} = P_{\text{ram}} + P_{\text{before}}. \quad (34)$$

As we mentioned, the thermal diffusivity is high, so the temperature jump across the shock is very small. As a result, the radiation pressure is nearly the same on either side of the shock, so Equation (34) relates the gas pressure before and after.

The ram pressure due to inflows is

$$P_{\text{ram, inflow}} \approx \rho v^2 \approx \frac{GM_* \rho}{R_*}. \quad (35)$$

When the AGN star loses mass, there is a similar term accounting for the force required to launch the outflow:

$$P_{\text{ram, outflow}} = \rho_{\text{outflow}} v_{\text{esc}}^2 = \frac{\dot{M}_{\text{Edd}} v_{\text{esc}}}{4\pi R_*^2}. \quad (36)$$

To ensure that this boundary condition smoothly reduces to the usual Eddington atmospheric condition, we also add a contribution $(1/3)aT_*^4 + g/\kappa_{\text{surface}}$, so in full we have

$$P_{\text{surf}} = \frac{1}{3}aT_*^4 + \frac{GM_* \rho}{R_*} + \frac{\dot{M}_{\text{Edd}} v_{\text{esc}}}{4\pi R_*^2} + \frac{g}{\kappa_{\text{surface}}}, \quad (37)$$

where P_{surf} is the pressure in the outermost cell of the MESA model. Note that we neglect the gas and radiation pressure in the accretion stream and just use the ram pressures because we have assumed that the stream is not pressure supported and hence that the total ram pressure exceeds the gas and radiation pressures.

5. Numerical Implementation

We implemented the physics described in Section 4 using the Modules for Experiments in Stellar Astrophysics (MESA; Paxton et al. 2011, 2013, 2015, 2018, 2019) software instrument. Details of the numerical implementation, together with the microphysics inputs to this software instrument, are given in Appendix B.

In the next section, we show calculations of AGN star evolution with ambient conditions $c_{s, \text{AGN}}$ and ρ_{AGN} as derived in Section 3. We also verify that in our MESA implementation the evolution of AGN stars reduces to classic stellar evolution for $(T_{\text{AGN}}, \rho_{\text{AGN}}) \rightarrow 0$.

The most important physics affecting the evolution of AGN stars is accretion. The initial accretion rate depends on the AGN conditions $c_{s, \text{AGN}}$ and ρ_{AGN} and the initial mass of the star. For numerical reasons, we assume an initial time of 10^4 yr, during which the accretion rate slowly increases to the Bondi value and the canonical surface-boundary conditions are blended with the modified boundary conditions described in Section 4.5. All of our models begin with an initial mass of $1M_\odot$ and an initial metallicity of $Z=0.02$. We find that different choices of initial mass $M > 1M_\odot$ do not change our results significantly.

For these models, we also assume that AGN stars remain at constant $c_{s, \text{AGN}}$ and ρ_{AGN} throughout their lives, and that the composition of accreted material is constant with $X=0.72$, $Y=0.28$, and $Z=0$. Different compositions of the accreted

material might change the results, and we will explore this effect in future work. We do not account for migration through the disk or stellar feedback beyond the super-Eddington winds accounted for in our models (Section 4.2).

6. Results

Three important timescales regulate the evolution of AGN stars: the accretion timescale $\tau_B = M_*/\dot{M}_B$, the nuclear timescale $\tau_{\text{Nuc}} \approx 0.007 M_* c^2 / L_*$, and the AGN lifetime τ_{AGN} . The evolution of AGN stars is dictated by the hierarchy of these timescales.

6.1. Slow Accretion

When $\tau_B > \tau_{\text{Nuc}}$ or $\tau_B > \tau_{\text{AGN}}$, AGN stars accrete small or negligible amounts of mass. Their evolution is not substantially altered, but depending on the AGN disk conditions a population of low- and intermediate-mass stars with AGN-like photospheric chemistry could be formed. This population of long-lived AGN stars is interesting because it could provide observational tests of the theory as well as a probe of former AGN conditions (see Section 7).

6.2. Intermediate Accretion

When $\tau_{\text{Nuc}} \lesssim \tau_B < \tau_{\text{AGN}}$, the accretion timescale is comparable to the burning timescale. AGN stars in these circumstances initially become massive via accretion, but continue to burn hydrogen faster than they accrete fresh fuel. As a result, these stars evolve to late nuclear-burning stages. As they become massive, due to their enhanced internal mixing (see Section 4), they also tend to evolve quasi-chemically homogeneously (Maeder 1987). Eventually, these AGN stars reach the Eddington luminosity, at which point they tune themselves to sit near $L_* = L_{\text{Edd}}$. This happens because on one hand mass loss reduces L_*/M_* , while on the other hand the chemical evolution of the core serves to increase L_*/M_* . The gradual increase in the stellar mean molecular weight increases the Eddington ratio L_*/L_{Edd} , so once the star reaches the Eddington limit, it will be forced to constantly lose mass in order to keep near $L_* = L_{\text{Edd}}$ (Owocki & Shaviv 2012). During their evolution, these well-mixed stars produce and then expel significant quantities of nuclear ash, which can serve to chemically enrich the AGN disk (Section 7.1). Our intermediate accretion calculations reach late phases of nuclear burning (typically oxygen burning) as H-free, compact stars with $M_* \approx 10 M_\odot$. These stars are expected to undergo core collapse and produce compact remnants (Section 7.2). In our model grid with $c_{s, \text{AGN}} = 10 \text{ km s}^{-1}$, we predict that stars lie in this regime when $\rho_{\text{AGN}} \simeq 5 \times 10^{-18}$ to $8 \times 10^{-19} \text{ g cm}^{-3}$ (tracks ending with a star symbol in Figure 8).

6.3. Runaway Accretion

When $\tau_B \ll \tau_{\text{Nuc}} < \tau_{\text{AGN}}$, AGN stars rapidly become massive. Due to their enhanced internal mixing (see Section 4), these models stay quasi-chemically homogeneous, and hydrogen-rich material accreted from the surface is efficiently mixed in the stellar core. Because $\tau_{\text{Nuc}} \gg \tau_B$, the star is supplied with fresh fuel at a rate faster than it can burn it. Therefore, the evolution stalls on the main sequence, and the runaway accretion process results in a supermassive star ($M_* \gg 100 M_\odot$). These stars reach masses of about $1000 M_\odot$.

before super-Eddington mass loss starts balancing accretion. Being so massive, these models are almost fully convective and stay chemically homogeneous since we assume mixing is very efficient also in radiative regions of stars close to the Eddington limit (Section 4.4). In this situation, the stellar core is continuously supplied by fresh fuel from the AGN disk, and the main-sequence lifetime of the model can be extended indefinitely (as long as the accretion rate remains high enough).

We evolve these models for some time to show this peculiar evolutionary feature of AGN stars. Some show interesting oscillations of their maximum mass around a mean value that appear stochastic, but since this is likely dependent on the uncertain implementation of mass loss and accretion close to the Eddington limit, we did not investigate this feature in depth. Models at the highest range of the accretion rates explored in this work tend to terminate for numerical reasons when they approach $\approx 1000 M_{\odot}$, so it is difficult to predict the final outcome of models at higher densities or lower sound speeds. However, it seems plausible that for such conditions AGN star models would still undergo a runaway accretion phase and reach equilibrium masses $\sim 10^3 M_{\odot}$, just on shorter timescales.

We predict that AGN stars lie in this runaway accretion regime when $\rho_{\text{AGN}} > 5 \times 10^{-18} \text{ g cm}^{-3}$ and $c_{s,\text{AGN}} = 10 \text{ km s}^{-1}$ (tracks ending with triangles in Figure 8 and 9), as well as for $\rho_{\text{AGN}} > 1.5 \times 10^{-19} \text{ g cm}^{-3}$ in models with $c_{s,\text{AGN}} = 3 \text{ km s}^{-1}$ (see Figure 17). AGN star models with $c_{s,\text{AGN}} = 100 \text{ km s}^{-1}$ require much higher values of density to become supermassive ($\rho_{\text{AGN}} > 5 \times 10^{-15} \text{ g cm}^{-3}$); see the model grids in Figures 19 and 20. For $c_{s,\text{AGN}} = 10 \text{ km s}^{-1}$, the models that become supermassive require between 4 and 50 Myr to do so. Since $\dot{M}_{\text{B}} \propto \rho_{\text{AGN}} c_{s,\text{AGN}}^{-3}$, this time decreases substantially for lower values of the AGN sound speed.

If we artificially interrupt accretion, mimicking the star exiting the AGN or entering a gap, or the AGN dissipating altogether (e.g., for $t > \tau_{\text{AGN}}$), models can evolve to later nuclear-burning phases. This results in the ratio L_*/M_* staying close to the Eddington limit, which leads to significant mass loss (Equation (16)). Their evolution is almost identical to what is described in Section 6.2, and the end state for these models is also core collapse as H-free, compact stars of $\approx 10 M_{\odot}$. In Section 7.2 we discuss the type of stellar explosions and compact remnants these AGN stars might produce.

Note that Goodman & Tan (2004) and Dittmann & Miller (2020) also reported the possibility of producing massive and supermassive stars in AGN disks. The main difference from our scenario is that they focused on in situ formation, while we are agnostic to the mechanism producing stellar seeds in AGN disks. Similar to their study, the maximum mass of our AGN stars is set by their ability to halt accretion via feedback, although in our case stars only reach masses of $\approx 1000 M_{\odot}$.

6.4. Massive and Very Massive Stars in the Inner Regions of AGNs

Our results show that the inner regions of AGN disks are likely populated by a large number of massive and very massive stars. The total number of massive stars that an AGN disk can produce via accretion onto low-mass stars formed in situ or captured from nearby nuclear clusters depends on the AGN properties, in particular its density, sound speed, and lifetime. We have shown that for values of the sound speed $\leq 10 \text{ km s}^{-1}$, runaway accretion occurs for densities higher than $\approx 10^{-17} \text{ g cm}^{-3}$. In this case, AGN stars reach

masses above $100 M_{\odot}$ in less than 10 Myr, with the accretion timescale decreasing rapidly for higher values of the density and lower values of the local sound speed.

It is conceivable that accretion is eventually halted via some feedback process, or the star entering regions of the disk with much lower values of density (or much larger values of sound speed), or the AGN shutting off altogether. We attempted to simulate this occurrence by suddenly decreasing the local density by a factor of 10^5 for a model of an AGN star initially evolved at $\rho_{\text{AGN}} = 2 \times 10^{-18} \text{ g cm}^{-3}$ and $c_{s,\text{AGN}} = 3 \text{ km s}^{-1}$. In this case, the evolution of the stellar model proceeds to later nuclear-burning stages, and a large fraction of accreted material is removed via a super-Eddington wind (Figures 10 and 11). This material has been processed by high-temperature nuclear burning, so it is returned to the AGN highly enriched in helium and metals (Figure 15). We discuss in Section 7.1 the implications of the presence of such thermonuclear factories in AGN disks. These massive AGN stars are also expected to leave behind a large population of compact remnants in the inner regions of AGN disks, and we discuss possible observational consequences in Sections 7.2 and 7.3.

7. Observational Signatures

Here we discuss possible observational signatures of AGN star evolution. We focus on the predicted chemical enrichment of the host AGN, the type of stellar populations that might be left in galactic centers, and the stellar explosions and compact remnants resulting from this exotic stellar evolution pathway. Compact remnants in AGN disks are particularly interesting as progenitors of gravitational wave sources, and we briefly discuss the impact of our scenario for this production channel.

7.1. AGN Pollution

While measurements of abundances in AGNs are very difficult and depend on detailed model assumptions (Maiolino & Mannucci 2019), the consensus is that both high- and low-redshift AGNs appear to have solar-to-supersolar metallicities (e.g., Storch Bergmann & Pastoriza 1989; Hamann et al. 2002; Jiang et al. 2018a; Maiolino & Mannucci 2019). Despite careful and extensive searches, low-metallicity AGNs seem to be extremely rare (Groves et al. 2006).

AGN stars provide a potential explanation for this observational puzzle. Because they tend to be longer lived (due to rejuvenation) and more efficiently mixed than ordinary massive stars, AGN stars are able to process more hydrogen and helium into metals. Moreover, they lose large amounts of mass due to the interplay of accretion and mass loss occurring when they reach their Eddington luminosity (Figure 5). The composition of the material lost by an AGN star model as a function of time is shown in Figure 12. This model was evolved until oxygen burning. While the material that falls onto the star is 72% H and 28% He, the material that is lost to the AGN disk is 36.6% H, 61.7% He, and 1.7% metals by mass (see cumulative yields in Figure 13). Most of the metals are produced toward the end of this model's evolution, and real AGN stars may provide further AGN enrichment via supernova explosions and gamma-ray bursts (GRBs). We tested the effect of adopting different mixing efficiencies on the yields by choosing different values for ξ in Equation (20) ($\xi = [2, 4, 7]$) and found differences of less than 2%.

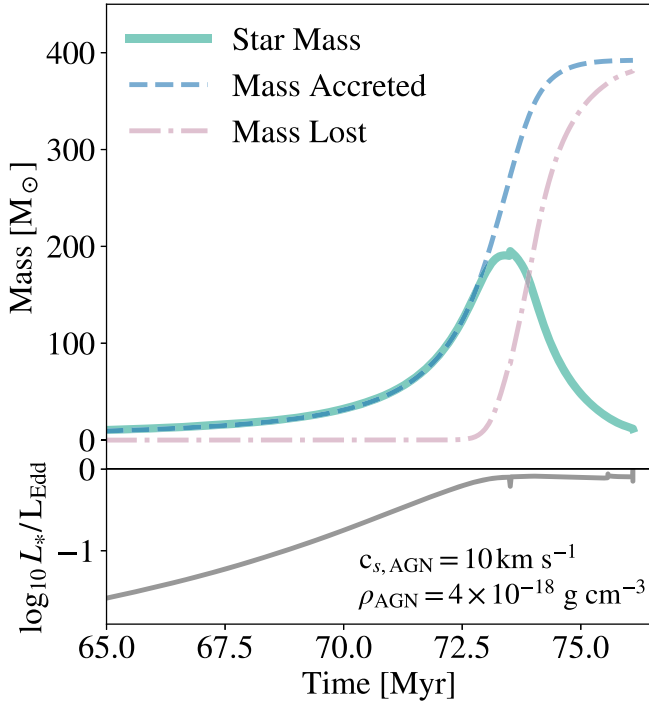


Figure 5. Mass budget for an AGN star model evolved at a density of $4 \times 10^{-18} \text{ g cm}^{-3}$ and a temperature of about 186 K (AGN sound speed of 10 km s^{-1}). For the last $\approx 12 \text{ Myr}$ of the calculation, we show the evolution of the model’s total mass (green curve), cumulative accreted mass (blue dashed line), and cumulative mass lost (purple dashed–dotted line). In the lower panel, we also show the time evolution of the Eddington ratio.

Note that AGN star models evolved at higher accretion rates can pollute the disk on much shorter timescales. For example, models initially experiencing runaway accretion but eventually entering regions of the disk with lower densities or sound speed rapidly evolve and lose large quantities of chemically enriched material. This is the case for the model shown in Figure 11, which released about $89.2 M_{\odot}$ of He and several solar masses of metals in less than 7 Myr (Figures 14 and 15). Finally, we want to stress that the yields shown in Figures 12 and 15 are just typical examples, and AGN stars with different disk conditions can produce different outcomes.

To determine whether or not the helium pollution we predict is significant relative to the overall mass budget of the AGN disk, note that the accretion rate in the disk is given by Equation (A5) as $2m_8 M_{\odot} \text{ yr}^{-1}$. By contrast, our models show that typical massive AGN star models enhance the primordial material of the AGN disk at an average rate of 10^{-4} to $10^{-5} M_{\odot} \text{ yr}^{-1}$. This suggests that a population of 10^4 – 10^5 AGN stars would suffice to produce significant helium enrichment in the disk. This calculation is complicated somewhat by the different outcomes of AGN star evolution in different density and temperature regimes, but it provides the order-of-magnitude population that would be required for the chemical enrichment to be significant.

7.2. Stellar Explosions and Compact Remnants

The main feature of AGN star evolution is the possibility of growing to large masses via accretion and evolving toward core collapse. We expect the relative yields of core-collapse supernovae, GRBs, and compact remnants in the inner regions

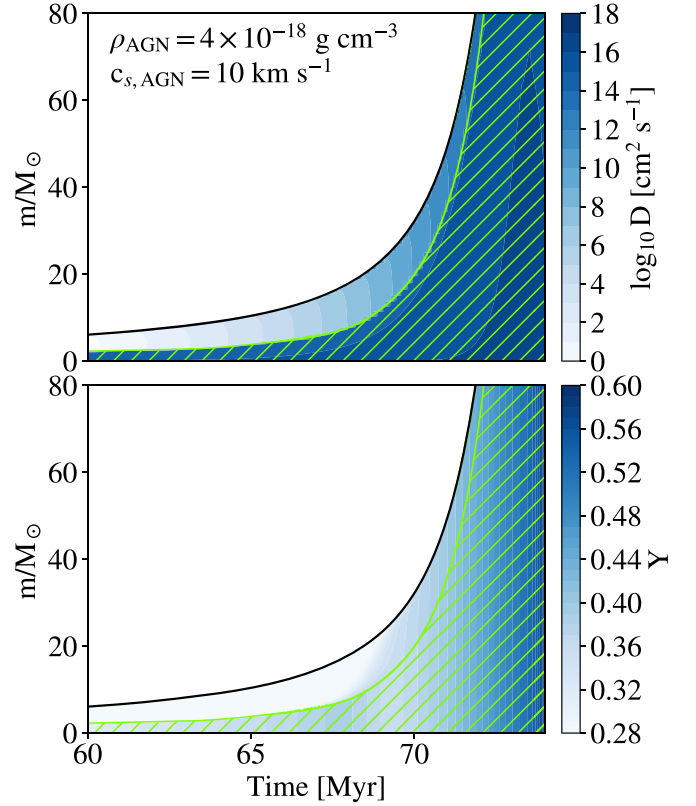


Figure 6. Zoom-in on the evolution of an AGN star model at a density and ambient sound speed of $4 \times 10^{-18} \text{ g cm}^{-3}$ and 10 km s^{-1} , respectively. The Kippenhahn plots show the increasing role of internal mixing as the stellar mass increases. In the upper panel, the blue shading shows the magnitude of the compositional diffusivity D (in $\text{cm}^2 \text{ s}^{-1}$), which is always large in convective regions (green hatched) and increases in radiative regions as the star approaches the Eddington limit (see Equation (20)). In the lower panel, the shading indicates the helium mass fraction (Y).

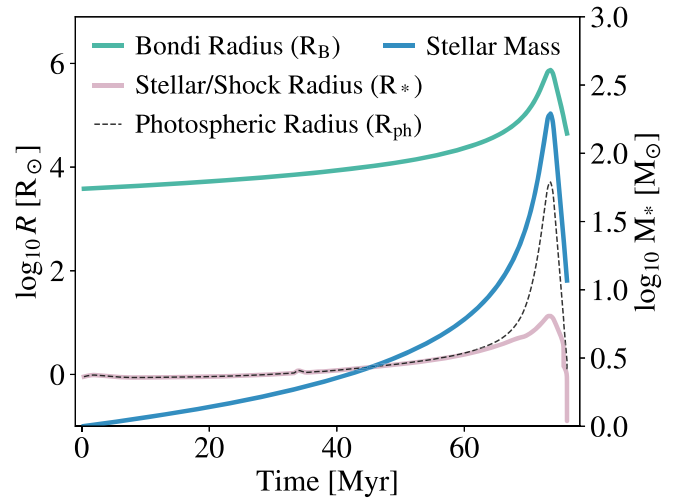


Figure 7. Time evolution of relevant radii for the problem of a star evolving in an AGN disk. The largest radius is always the Bondi radius (Equation (14)). The outer boundary of the MESA calculation is placed at the shock radius, where the infalling material slows from supersonic to subsonic. The photospheric radius (Equation (33)) corresponds to the shock radius for small accretion rates, but can grow up to the Bondi radius for large accretion rates. Values of these radii are shown, together with total stellar mass, for an AGN star model at a density and ambient sound speed of $4 \times 10^{-18} \text{ g cm}^{-3}$ and 10 km s^{-1} , respectively.

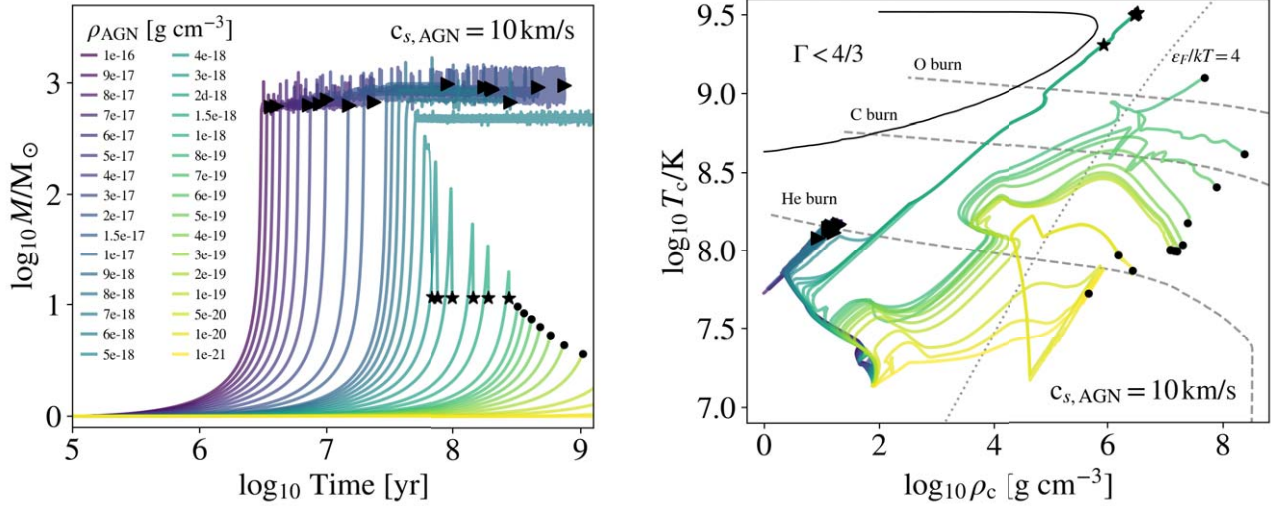


Figure 8. Grid of stellar models evolved with a fixed AGN sound speed of 10 km s^{-1} and AGN densities ranging from 10^{-16} to $10^{-21} \text{ g cm}^{-3}$. Left panel: evolution of stellar mass as a function of log time for models starting with $M = 1M_{\odot}$. Models evolving at densities higher than $\approx 5 \times 10^{-18} \text{ g cm}^{-3}$ experience runaway accretion and become supermassive stars. Models evolving at densities $5 \times 10^{-18} \leq \rho_{\text{AGN}} \leq 8 \times 10^{-19} \text{ g cm}^{-3}$ become massive stars before losing mass via super-Eddington winds and ending their lives with $M \approx 10M_{\odot}$ (tracks ending with a star symbol). At densities lower than $\approx 5 \times 10^{-19} \text{ g cm}^{-3}$, models end their main-sequence evolution before accreting sufficient material to become massive stars ($M \lesssim 8M_{\odot}$, tracks ending with a circle). Right panel: evolution in the central density–central temperature plane. Runaway models are continuously replenished via accretion and burn hydrogen indefinitely (triangles). Intermediate accretion models evolve to late burning stages (tracks ending with star symbols). AGN star evolution reduces to classic stellar evolution for very small values of ρ_{AGN} (small accretion rates). Dashed lines show the ignition location of different nuclear fuels. The pair-instability region is shown as a continuous black line, while the dotted line shows the transition to electron-degenerate gas.

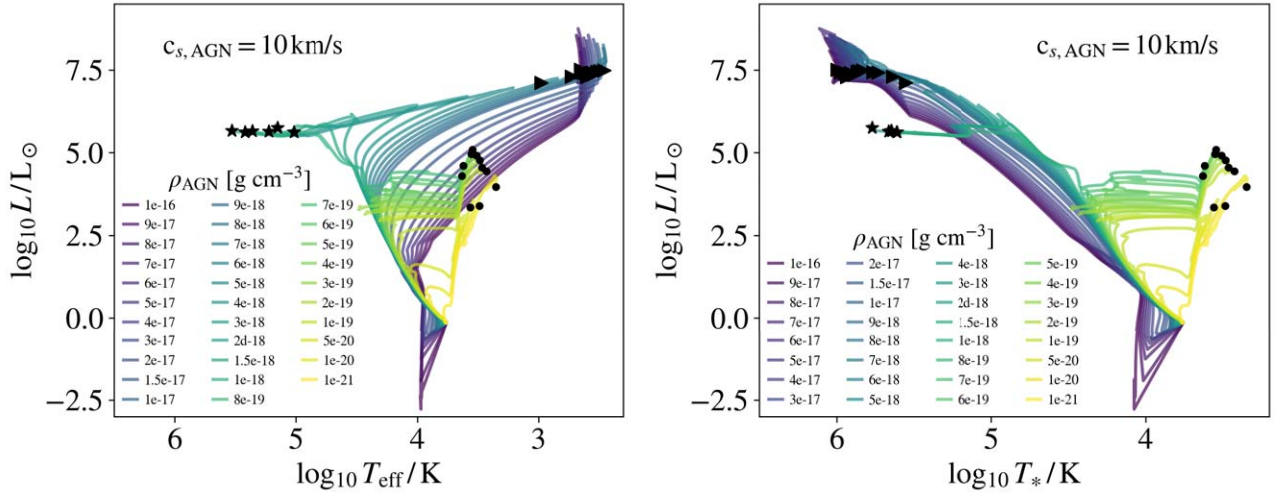


Figure 9. Evolution on the Hertzsprung–Russell diagram for the models shown in Figure 8. Left panel: the effective temperature of the models is calculated assuming electron-scattering opacity for the accretion stream. This is the temperature of the star for an observer sitting at the Bondi radius. Right panel: same as left panel, but using the surface temperature of the MESA model instead of the effective temperature (Equation (30)). This diagram is useful to understanding the type of evolution that AGN star models are undergoing, as compared to canonical stellar evolution.

of AGNs to be much larger than what is anticipated for a stellar population with a standard initial mass function (IMF). The light from some of these explosive events might be detectable even if it occurs inside AGN disks (Perna et al. 2021; Zhu et al. 2021).

In our models, the interplay of accretion and mass loss (see Section 4.2) results in massive AGN stars evolving such that their ratio L_{*}/M_{*} approaches and stays at the Eddington limit. For an initial stellar metallicity of $Z = 0.02$, we find that AGN stars that accrete large amounts of mass subsequently lose most of their mass before reaching core collapse. The strong mass-loss rates and enhanced mixing experienced by these stars cause them to reach core collapse as compact, H-free stars with

$M_{*} \approx 10M_{\odot}$. In order to predict their likely outcome after core collapse, we compare with the predictions of Ertl et al. (2020), who looked at the explodability of helium stars. The presupernova structures of our models allow us to calculate their compactness parameter (e.g., O’Connor & Ott 2011; Sukhbold & Woosley 2014), which we then use to predict if the star produces a successful explosion and what kind of compact remnant is left behind. Since the nuclear network adopted during late phases of burning can affect the presupernova structure and its core compactness (Farmer et al. 2016), we calculated a few models adopting a larger nuclear network (mesa_128.net, which uses 128 isotopes). While a systematic study of the compactness parameter of AGN stars will be performed in a

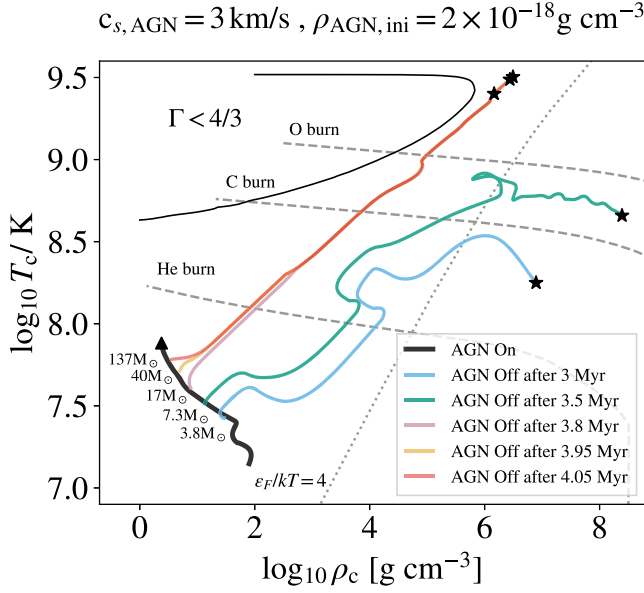


Figure 10. Evolution of AGN star models in the central density–central temperature plane for different AGN lifetimes. A $1 M_{\odot}$ model accretes rapidly at $\rho_{\text{AGN}} = 2 \times 10^{-18} \text{ g cm}^{-3}$ and $c_{s,\text{AGN}} = 3 \text{ km s}^{-1}$, becoming a $785 M_{\odot}$ supermassive star in about 4.1 Myr. Halting the accretion before this point results in different evolutionary pathways. If the initial AGN conditions persist for more than ≈ 3.5 Myr, the models produce massive stars that undergo core collapse.

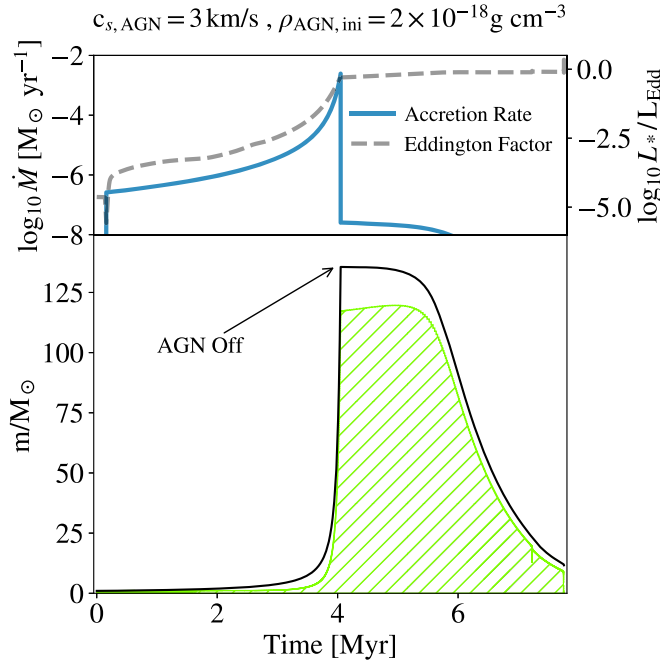


Figure 11. A $1 M_{\odot}$ model accretes rapidly at $\rho_{\text{AGN}} = 2 \times 10^{-18} \text{ g cm}^{-3}$ and $c_{s,\text{AGN}} = 3 \text{ km s}^{-1}$. We simulate the shutoff of the AGN (or the migration of the AGN star into a gap) by decreasing the local density by a factor of 10^5 after 4.05 Myr. The model stops accreting substantial amounts of mass and evolves past the main sequence (red curve in Figure 10). Similar to intermediate accretion models, the luminosity stays close to the Eddington limit for most of the subsequent evolution, resulting in large values of the mass-loss rate. After about 7 Myr, the model ends its life as a compact He star of $\approx 10 M_{\odot}$. Hatched green regions in the lower panel are convective.

subsequent work, in these models we found compactness parameters above 0.2, which when compared with the results of Ertl et al. (2020) suggest they should produce a BH. These

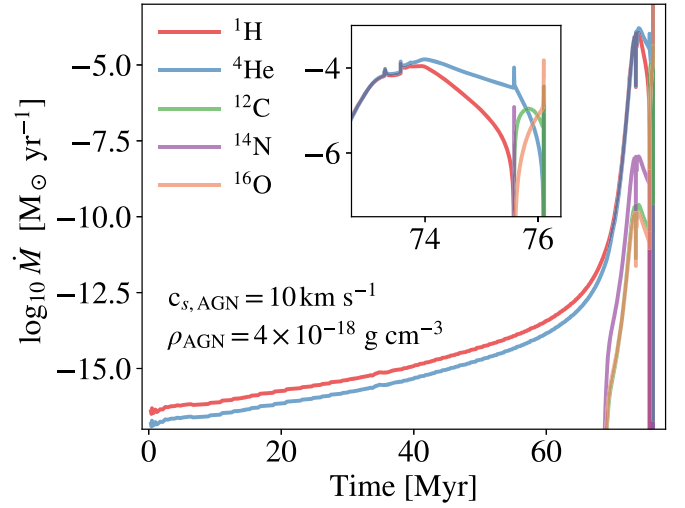


Figure 12. The mass lost by an AGN star model is shown broken down by species as a function of time. This model was evolved at a density of $4 \times 10^{-18} \text{ g cm}^{-3}$ and a temperature of about 186 K (AGN sound speed of 10 km s^{-1}). The first part of the evolution is dominated by accretion, and material is lost from the star at a very small rate. As the star approaches the Eddington limit, enhanced mixing dredges processed material up from the core, and super-Eddington winds then eject large amounts of helium-rich material. As the star evolves to the late burning stages, it also loses material rich in carbon and oxygen.

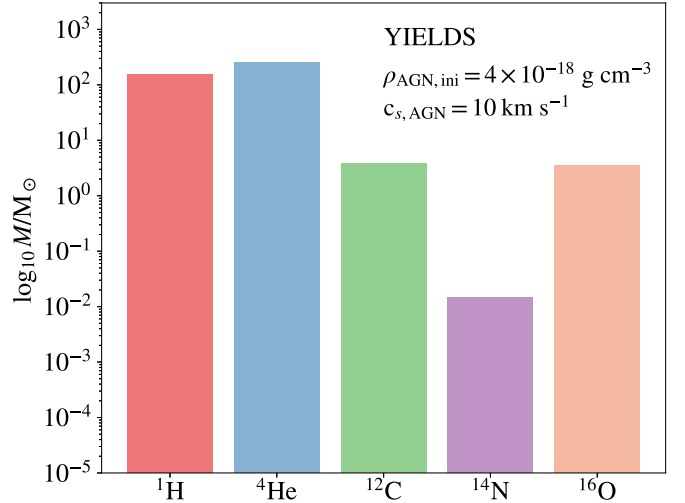


Figure 13. Cumulative yields corresponding to the mass lost by the intermediate accretion model in Figure 12. Throughout its lifetime (≈ 77 Myr), this model releases in the AGN $153.4 M_{\odot}$ of H, $258.6 M_{\odot}$ of He, $3.8 M_{\odot}$ of C, $0.015 M_{\odot}$ of N, and $3.47 M_{\odot}$ of O. This is just accounting for stellar mass loss. A supernova explosion would enhance these yields further and would do so mostly for heavier elements.

BHs can further accrete and merge, with important implications for gravitational wave sources, as well as low-mass and high-mass X-ray binaries and GRBs in the inner regions of galaxies. A population of energetic explosions embedded in AGNs could result in important feedback effects on disk accretion and structure and possibly explain some AGN variability (e.g., Graham et al. 2017).

7.3. Gravitational Wave Sources

The gravitational wave events detected by LIGO-Virgo might originate from stellar-mass binary black hole (BBH) mergers in AGN disks (see, e.g., McKernan et al. 2012, 2014;

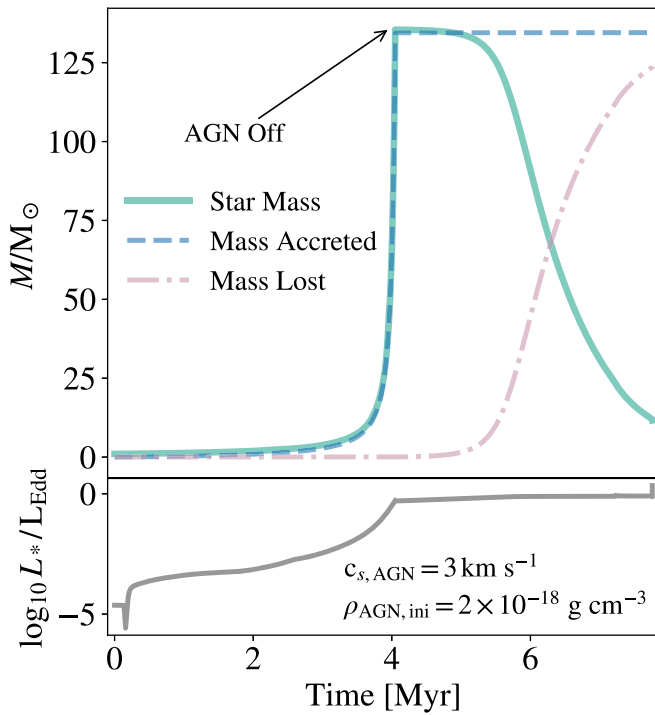


Figure 14. Mass budget for the model in Figure 11. Through its lifetime (≈ 7 Myr), this model accreted from the AGN disk about $134 M_{\odot}$ of gas and released in the AGN approximately $125 M_{\odot}$ of nuclearily processed material.

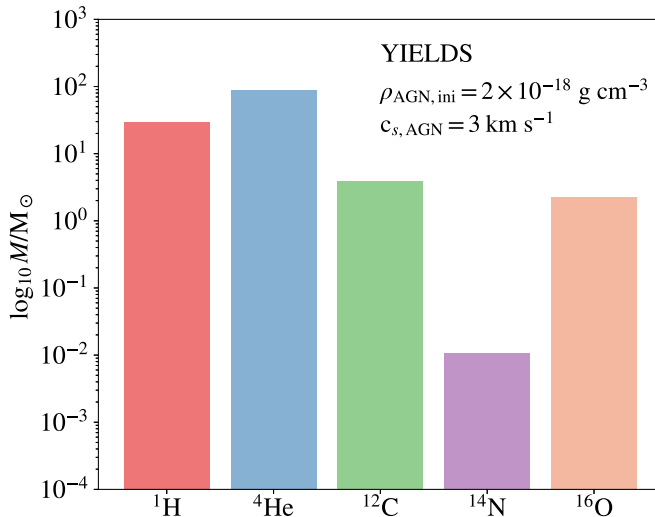


Figure 15. Cumulative yields corresponding to the mass lost by the model in Figure 11. This is a runaway accretion model that experienced a shutoff of the AGN (or entered a gap) after 4.05 Myr. Throughout its lifetime (≈ 7 Myr), this model releases in the AGN $29.6 M_{\odot}$ of H, $89.2 M_{\odot}$ of He, $3.84 M_{\odot}$ of C, $0.011 M_{\odot}$ of N, and $2.29 M_{\odot}$ of O. This is just accounting for stellar mass loss. A supernova explosion would enhance these yields further and would do so mostly for heavier elements.

Bartos et al. 2017; Stone et al. 2017; Graham et al. 2020). The recent detection of a BBH merger with at least one BH formed in the pair-instability mass gap supports formation channels requiring (multiple) stellar coalescences or hierarchical mergers of lower mass black holes in AGNs or star clusters (GW190521, Abbott et al. 2020a, 2020b).

For the “AGN channel,” the expected merger rate is usually parameterized assuming an initial distribution of BHs and stars surrounding the central SMBH, with the BHs formed either in a

Toomre-unstable AGN disk or in a nuclear stellar cluster (Stone et al. 2017; McKernan et al. 2018; Fragione et al. 2019; Tagawa et al. 2020). In our scenario, most compact remnants descend from initially low-mass stars that are either captured or formed by the AGN disk, and in regions where the accretion rate is sufficiently high they become massive in a timescale shorter than typical AGN lifetimes (1–100 Myr, e.g., Haiman & Hui 2001; Martini & Weinberg 2001; Khrykin et al. 2019). Regardless of the details of star formation in the regions surrounding SMBHs, this process is likely mimicking the effects of having a particularly top-heavy IMF in the inner regions of the AGN disk. Our results show that a large population of compact remnants could be produced within AGNs in regions of the disk where the accretion rate is sufficiently high.

The evolution of these compact remnants in AGNs is dominated by a number of processes: disk migration and binary formation (Bellovary et al. 2016; Secunda et al. 2019; Tagawa et al. 2020), hardening via three-body scattering and gaseous drag (Stone et al. 2017; Leigh et al. 2018), gas accretion and mergers (Yang et al. 2020), and disk–binary interaction (Gröbner et al. 2020; Ishibashi and Gröbner 2020). While the details are complex, the literature supports the possibility of forming larger and larger BH pairs via hierarchical merger and accretion of a seed BH population, eventually allowing the production of intermediate-mass black holes in AGNs. Our work strengthens this suggestion by providing a mechanism to rapidly and efficiently populate the inner regions of AGNs with compact remnants.

7.4. The Galactic Center

An interesting application of AGN star evolution is the ability to constrain AGN disk parameters and physics using some of the predictions for the type of remnants, stellar explosions, and GW sources expected from this peculiar stellar evolution channel. While the space parameter of AGN lifetime, density, and sound speed is degenerate, it is likely that progress could be made by pairing different observational proxies. This route could be particularly interesting for studying the Galactic Center (GC), where observations of stellar populations and stellar remnants are directly available.

There is strong evidence for the existence of a central massive black hole of $\approx 4 \times 10^6 M_{\odot}$ in the Milky Way (Genzel et al. 2010). While the accretion rate onto this SMBH is currently low, observations suggest that Sgr A* was much brighter in the recent past (Su et al. 2010). If the Milky Way experienced an AGN phase not too long ago, the properties of the stellar populations and remnants currently observed in the GC can be used to test some of the ideas discussed in this paper.

The central parsec contains about 200 young, massive stars. The presence of so many young stars in the immediate vicinity of the central black hole is unexpected (Ghez et al. 2003b; Alexander 2005). The surface density of a group of massive O/WR stars in the inner 1 pc region increases steeply from $\sim 13''$ (0.5 pc) to a few arcseconds, with no O/WR stars observed beyond 0.5 pc (Paumard et al. 2006; Bartko et al. 2010). Another group of early-type B stars (S-star cluster) shows a similar sharp inward increase of its surface density (Bartko et al. 2010). Stellar spectroscopy shows that some of these stars might be He-rich (Martins et al. 2008; Habibi et al. 2017; Do et al. 2018). There is evidence that the present-day stellar mass

function (PMF) for the group of centrally concentrated O/WR stars is flat, and it becomes steeper when moving farther out (Paumard et al. 2006; Bartko et al. 2010). The agreement is that the PMF within 0.5 pc is top-heavy (Genzel et al. 2010).

The two-body relaxation timescale in the central parsec ranges between 1 and 20 Gyr, much longer than the lifetime of the B and O/WR stars (Alexander 2005), so this central concentration of massive stars cannot be a Bahcall–Wolf cusp (Bahcall & Wolf 1976, 1977). On the other hand, lower mass old stars do not exhibit this central concentration; their distribution flattens close to the GC (Genzel et al. 2010; Do et al. 2017). This is contrary to basic theoretical predictions (Bahcall & Wolf 1976, 1977). A number of mechanisms have been proposed to account for the anomalous properties of the stellar population in the GC, including in situ star formation and in-spiraling of a star cluster (see Genzel et al. 2010 for a review of these scenarios and their challenges). In the context of AGN star evolution, the observations could be explained by low-mass stars accreting large amounts of mass in the inner ≈ 1 pc region of an AGN disk some ~ 6 Myr ago. This could naturally account for the surface densities of the different stellar populations, a radially dependent, top-heavy PMF, and chemical peculiarities observed in some of the B-star spectra.

The low-mass X-ray binary candidates identified in the galactic center by Hailey et al. (2018) are found only within ≈ 1 pc. A possible explanation of this peculiar distribution relies on the migration of compact remnant binaries formed via a gas-capture mechanism during a former AGN phase (Tagawa et al. 2020). However, in the context of AGN star evolution, the 1 pc cutoff could simply represent the radial distance beyond which the gas conditions did not allow for enough accretion to form massive and very massive stars. Beyond this radius, stars can still accrete substantial amounts of mass, but they did not evolve toward core collapse. Owing to their longer evolutionary timescales, some of these intermediate-mass objects could still be present in the GC, possibly showing spectroscopic signatures of accreted AGN material (Cunha et al. 2007; Martins et al. 2007, 2008; Habibi et al. 2017; Do et al. 2018; see Section 7.1).

8. Conclusions

Stellar evolution in AGN disks proceeds quite differently than in a vacuum. Depending on the density and sound speed of the gas in which they are embedded, abundant low-mass stellar seeds provided either via capture or in situ formation can rapidly accrete and become massive or supermassive stars. These stars have large convective cores, and their luminosity approaches the Eddington limit, so their interiors are prone to mixing. The interplay between accretion and mass loss is likely to enforce envelope circulations, with the mixing timescale decreasing rapidly as the star grows in mass. Therefore, we expect AGN stars that accrete substantial amounts of mass to evolve quasi-chemically homogeneously (Maeder 1987; Yoon & Langer 2005), their surface composition largely reflecting the composition of their nuclear-burning cores. AGN stars evolving as massive and very massive stars are expected to lose large amounts of mass enriched in helium and CNO-processed elements. When evolving to core collapse, they can also expel large amounts of heavy elements via SN explosions, further polluting their AGN disk. Overall, the metallicity of AGNs is expected to increase rapidly in the presence of AGN stars.

Due to the efficiency of internal mixing, AGN stars that become massive and very massive are only able to evolve when the accretion-rate timescale becomes comparable to or longer than the nuclear-burning timescale. Depending on the values of density and sound speed of the medium in which they are embedded, our AGN star models are in this regime from the beginning of the calculation, or they enter it when the accretion rate decreases substantially with a change in the AGN disk conditions. This could be due to the end of the AGN phase or the star migrating to regions of the disk with different gas conditions (e.g., gaps). Our AGN star models that accreted large amounts of mass eventually end their evolution as compact, H-free stars of about $10 M_{\odot}$ that undergo core collapse. This outcome is caused by the interplay of accretion and mass loss, which in our implementation keeps these chemically homogeneous stars evolving near $L_{*} = L_{\text{Edd}}$. Therefore, we expect AGN stars to efficiently populate AGN disks with compact remnants, to a rate much higher than what is expected from a population of stars with a canonical IMF. While we defer a thorough study of the parameter space of AGN stars to future works, the models computed for this paper point to an efficient production of compact remnants in the inner regions of AGN disks. These compact remnants are interesting seeds for the growth of BHs via further accretion or mergers, with important implications for the gravitational wave sources observed by LIGO-Virgo and for LISA predictions. A population of very massive stars and energetic explosions in the inner regions of galaxies could also have important consequences for the structure and accretion properties of AGNs.

We thank Alexander Dittmann, Saavik Ford, Yan-Fei Jiang, Yuri Levin, Barry McKernan, and Mathieu Renzo for useful discussions. We thank the anonymous reviewer, whose comments and suggestions helped improve and clarify this manuscript. The Center for Computational Astrophysics at the Flatiron Institute is supported by the Simons Foundation. This research was supported in part by the National Science Foundation under grant No. NSF PHY-1748958 and by the Gordon and Betty Moore Foundation through grant GBMF7392.

Software: MESA (Paxton et al. 2011, 2013, 2015, 2018, 2019), ipython/jupyter (Pérez and Granger 2007; Kluyver et al. 2016), matplotlib (Hunter 2007), NumPy (Harris et al. 2020), and Python from python.org.

Appendix A

Temperature and Density Ranges in AGN Disks

We adopt the conventional α -disk model (Shakura & Sunyaev 1973) for effective viscosity $\nu = \alpha h^2 \Omega R^2$, where $h = H/R$ is the aspect ratio, α is an efficiency factor for turbulent viscosity, and $\Omega (= GM_{\text{bh}}/R^3)^{1/2}$ is the angular frequency at a distance R from the SMBH. In a hydrostatic equilibrium, the disk scale height is

$$H = \frac{\sqrt{2}}{\Omega} c_{s,\text{AGN}} \simeq \frac{\sqrt{2}}{\Omega} \sqrt{\frac{R_g T_{\text{AGN,gas}}}{\mu}} \quad (\text{A1})$$

in the gas-pressure-dominated region and

$$H = \frac{\sqrt{2}}{\Omega} c_{s,\text{AGN}} \simeq \frac{4aT_{\text{AGN,rad}}^4}{3\Sigma\Omega^2} \quad (\text{A2})$$

in the radiation-pressure-dominated region. In the above expressions, $T_{\text{AGN,gas}}$ (or $T_{\text{AGN,rad}}$) is the midplane temperature,

$c_{s,\text{AGN}}$ is the midplane sound speed, and Σ is the surface density. The relative importance of radiation pressure P_{rad} compared to gas pressure P_{gas} is measured by

$$\beta_P = \frac{P_{\text{gas}}}{P_{\text{rad}}} = \frac{3R_g \rho_{\text{AGN}}}{\mu a T_{\text{AGN}}^3}, \quad (\text{A3})$$

which is generally smaller than unity in the outer regions of the disk.

In a steady state, the mass flux through the disk

$$\dot{M}_d = 3\pi\Sigma\nu \simeq 6\pi\alpha\rho_{\text{AGN}}h^3\Omega R^3 \quad (\text{A4})$$

where $\Sigma = 2\rho_{\text{AGN}}H$ and ρ_{AGN} are the surface density and midplane mass density. We use the most probable values of λ (~ 0.6) and ϵ (~ 0.06) for the Eddington factor and the mass-to-energy conversion efficiency, respectively (see Section 1). These are obtained from AGN evolution models (Shankar et al. 2009). We use these values to derive a \dot{M}_d – M_{bh} relationship and remove one degree of freedom for the input model parameters. We scale the SMBH’s mass by $m_8 \equiv M_{\text{bh}}/10^8 M_\odot$ and the distance in the disk from it by $r_{\text{pc}} \equiv R/1 \text{ pc}$ so that the Keplerian speed is $V_k \simeq 7 \times 10^2 m_8^{1/2} r_{\text{pc}}^{-1/2} \text{ km s}^{-1}$, the angular frequency $\Omega = 2.1 \times 10^{-11} m_8^{1/2} r_{\text{pc}}^{-3/2} \text{ s}^{-1}$, and the rate of mass accretion onto the SMBH

$$\dot{M}_{\text{bh}} \simeq \frac{\lambda f_m}{\epsilon} \frac{L_{\text{Edd}}}{C^2} \simeq 2f_m m_8 M_\odot \text{ yr}^{-1}, \quad (\text{A5})$$

where the factor f_m (~ 1) takes into account the dispersion in both λ and ϵ .

In conventional steady-state accretion-disk models (Shakura & Sunyaev 1973; Lynden-Bell & Pringle 1974), $\dot{M}_d \simeq \dot{M}_{\text{bh}}$, and the viscous dissipation provides a heating rate

$$Q^+ = 9\Sigma\nu\Omega^2/4 = 3\dot{M}_d\Omega^2/4\pi. \quad (\text{A6})$$

The cooling rate due to radiative diffusion in the direction normal to the disk is

$$Q^- = 2\sigma T_e^4 = 2\sigma T_{\text{AGN}}^4 \tau / (1 + \tau^2), \quad (\text{A7})$$

where T_c and T_e are the midplane and surface effective temperatures, respectively, and $\tau = \kappa\Sigma/2$ is the optical depth. In low-density AGN disks, the dominant source of opacity κ above $\sim 2 \times 10^3 \text{ K}$ is electron scattering $\kappa_{\text{es}} = 0.2(1+x) \text{ cm}^2 \text{ g}^{-1}$, where x is the ionization fraction (but see also Jiang et al. 2016). Below the sublimation temperature of the refractory grains, dust opacity dominates and $\kappa_{\text{dust}} \sim 0.1 T_{\text{AGN}}^{1/2} 10^{[\text{Fe}/\text{H}]} \text{ cm}^2 \text{ g}^{-1}$, where $[\text{Fe}/\text{H}]$ is the metallicity of the gas relative to the solar value (Bell & Lin 1994). For convenience, we approximate both κ_{es} ($\simeq 0.4 \text{ cm}^2 \text{ g}^{-1}$) and κ_{dust} ($\sim 4 \times 10^{[\text{Fe}/\text{H}]} \text{ cm}^2 \text{ g}^{-1}$) as constants.

In a thermal equilibrium, $Q^+ = Q^-$. Using Equation (A5), the effective temperature becomes

$$T_e = \left(\frac{3\dot{M}_{\text{bh}}\Omega^2}{8\pi\sigma} \right)^{1/4} \simeq 110 \frac{f_m^{1/4} m_8^{1/2}}{r_{\text{pc}}^{3/4}} \text{ K}. \quad (\text{A8})$$

Equations (A1) and (A4) lead to midplane temperature, density, and pressure

$$T_{\text{AGN,gas}} = \left(\frac{\kappa\mu\dot{M}^2\Omega^3}{16\pi^2\sigma\alpha R_g} \right)^{1/5} = T_g \left(\frac{\kappa\mu}{\alpha} \right)^{1/5} \frac{f_m^{2/5} m_8^{7/10}}{r_{\text{pc}}^{9/10}}, \quad (\text{A9})$$

$$\begin{aligned} \rho_{\text{AGN,gas}} &= \frac{\mu^{6/5}\Omega^{11/10}}{3R_g^{6/5}\alpha^{7/10}} \left(\frac{\dot{M}^4\sigma^3}{8\pi^4\kappa^3} \right)^{1/10} \\ &= \frac{\rho_g \mu^{6/5} f_m^{2/5} m_8^{19/20}}{\kappa^{3/10} \alpha^{7/10} r_{\text{pc}}^{33/20}}, \end{aligned} \quad (\text{A10})$$

$$P_{\text{gas}} = \left(\frac{\sigma}{2\kappa} \right)^{1/10} \left(\frac{\mu\dot{M}^2}{R_g\pi^2} \right)^{2/5} \frac{\Omega^{17/10}}{6\alpha^{9/10}} \quad (\text{A11})$$

with $T_g = 3.7 \times 10^3 \text{ K}$ and $\rho_g = 1.5 \times 10^{-13} \text{ g cm}^{-3}$ for the gas-pressure-dominated region and

$$T_{\text{AGN,rad}} = \left(\frac{c\Omega}{2\alpha\kappa} \right)^{1/4} = T_r \left(\frac{m_8}{\alpha^2\kappa^2 r_{\text{pc}}^3} \right)^{1/8} \quad (\text{A12})$$

$$\rho_{\text{AGN,rad}} = \frac{\pi^2 c^3}{3\alpha\kappa^3 \dot{M}_d^2 \Omega} = \frac{\rho_r r_{\text{pc}}^{3/2}}{\alpha\kappa^3 f_m^2 m_8^{5/2}}, \quad (\text{A13})$$

$$P_{\text{rad}} = \frac{c\Omega}{6\kappa\alpha}, \quad (\text{A14})$$

with $T_r = 2.6 \times 10^3 \text{ K}$ and $\rho_r = 2.2 \times 10^{-10} \text{ g cm}^{-3}$ for the radiation-pressure-dominated region. The solutions provide the T_{AGN} and ρ_{AGN} distributions for different values of M_{bh} and \dot{M}_d . From Equations (A3), (A9)–(A11), and (A12)–(A14), the boundary separating the gas- and radiation-pressure-dominated regions (where $\beta_P = 1$) occurs at

$$\begin{aligned} R_\beta &= \frac{(GM_{\text{bh}})^{1/3}(\alpha a)^{2/21}}{2^{2/7}(c/\kappa)^{6/7}} \left(\frac{\mu\dot{M}_d^2}{\pi^2 R_g} \right)^{8/21} \\ &= 0.09 \mu^{8/21} \kappa^{6/7} \alpha^{2/21} f_m^{16/21} m_8^{23/21} \text{ pc}. \end{aligned} \quad (\text{A15})$$

The gas pressure is dominant for $R < R_\beta$, whereas radiation pressure is dominant for $R > R_\beta$.

This steady-state, geometrically thin viscous disk model provides a useful estimate for the values of T_c and ρ_{AGN} (AGN midplane temperature and density). However, it is thermally unstable in the radiation-pressure-dominated region. Such an instability is incompatible with the thermal equilibrium assumption based on which the model is constructed (Pringle 1981). Moreover, these solutions suggest the possibility of gravitational instability in the outer regions of the disk.

Appendix B Software Details

Calculations were done with MESA version 15140. The `inlist` and MESA extensions required to reproduce the results in this work are available at [10.5281/zenodo.4437705](https://zenodo.org/record/4437705). The MESA equation of state (EOS) is a blend of the OPAL (Rogers & Nayfonov 2002), SCVH (Saumon et al. 1995), FreeEOS,⁷ HELM (Timmes & Swesty 2000), and PC (Potekhin & Chabrier 2010) EOSs. Radiative opacities are primarily from OPAL (Iglesias & Rogers 1993, 1996), with low-temperature data from Ferguson et al. (2005) and the high-temperature, Compton-scattering-dominated regime by Buchler & Yueh (1976). Electron conduction opacities are from Cassisi et al. (2007). Nuclear reaction rates are a combination of rates from NACRE (Angulo et al. 1999), JINA REACLIB (Cyburt et al. 2010), and additional tabulated weak

⁷ <http://freeeos.sourceforge.net/>

reaction rates from Fuller et al. (1985), Oda et al. (1994), and Langanke and Martínez-Pinedo (2000). Screening is included via the prescription of Chugunov et al. (2007). Thermal neutrino loss rates are from Itoh et al. (1996). We adopted a 21-isotope nuclear network (approx21.net), except for a few models where we tested the impact of adopting a 128-isotope network (mesa_128.net). Convective boundaries were modeled using the Schwarzschild criterion and no overshooting.

Appendix C Thermal and Advection Times

Our aim is to show that the thermal time for the accretion stream t_{th} is short compared with the advection time t_{adv} . Given that assumption, the full stellar luminosity must escape through the accretion stream, meaning that the stream carries $L = L_*$. The ratio between the two timescales is then

$$\frac{t_{\text{th}}}{t_{\text{adv}}} = \frac{m_{\text{above}} c_p T / L_*}{m_{\text{above}} / \dot{M}} = \frac{c_p \dot{M}}{L_*} = \frac{c_p \dot{M}}{L_{\text{Edd}}} \left(\frac{L_{\text{Edd}}}{L_*} \right), \quad (\text{C1})$$

where m_{above} is the mass above a given spherical shell and T is the temperature at the surface of the star. Letting κ be the opacity of the accreting material, we write

$$L_{\text{Edd}} = \frac{4\pi G M_* c}{\kappa} \quad (\text{C2})$$

and find with Equation (13)

$$\frac{t_{\text{th}}}{t_{\text{adv}}} = \frac{c_p T \kappa \eta R_B^2 \rho_{\text{AGN}} c_{s,\text{AGN}}}{G M_* c} \left(\frac{L_{\text{Edd}}}{L_*} \right). \quad (\text{C3})$$

Inserting Equation (14), we find

$$\frac{t_{\text{th}}}{t_{\text{adv}}} = \frac{4 c_p T \kappa \eta G M_* \rho_{\text{AGN}}}{c_{s,\text{AGN}}^3 c} \left(\frac{L_{\text{Edd}}}{L_*} \right). \quad (\text{C4})$$

With $c_p T \approx c_s^2$ and $\eta = 1$, we then write

$$\frac{t_{\text{th}}}{t_{\text{adv}}} = 2 R_B \kappa \rho_{\text{AGN}} \left(\frac{c_{s,\text{AGN}}}{c} \right) \left(\frac{c_s^2}{c_{s,\text{AGN}}^2} \right) \left(\frac{L_{\text{Edd}}}{L_*} \right). \quad (\text{C5})$$

Using $R_B \lesssim 10^{15} \text{ cm}$, $\rho_{\text{AGN}} \lesssim 10^{-14} \text{ g cm}^{-3}$, $\kappa \lesssim 1 \text{ cm}^2 \text{ g}^{-1}$, $c_{s,\text{AGN}}/c \lesssim 10^{-3}$, and $c_s/c_{s,\text{AGN}} < 10$, we find that this ratio is no more than

$$\frac{t_{\text{th}}}{t_{\text{adv}}} \lesssim \left(\frac{L_{\text{Edd}}}{L_*} \right). \quad (\text{C6})$$

In these extreme cases with large Bondi radii and high AGN densities, the luminosity quickly rises to Eddington in our models, so this ratio is at most unity, and it is a good approximation to let the entropy of the accreting material equal that of the surface of the model. In less extreme cases, L may be much less than L_{Edd} , but then the prefactor is much smaller and the approximation is again good (Paxton et al. 2015).

We could alternatively have assumed that the accretion stream is advection dominated and derived a contradiction. This proceeds as follows. The material that falls in adjusts to its new density adiabatically, following $\rho \propto r^{-3/2}$ (Equation (25)). The radiative luminosity the material carries is then given by

Equation (26) as

$$L = - \frac{64 \pi r^2 \sigma T^3}{3 \kappa \rho} \frac{dT}{dr}, \quad (\text{C7})$$

which implies a ratio of thermal time to advection time of

$$\frac{t_{\text{th}}}{t_{\text{adv}}} = \frac{3 \kappa \rho c_p \dot{M}}{64 \pi r^2 \sigma T^3} \frac{dr}{dT}. \quad (\text{C8})$$

For an ideal gas with $\gamma = 5/3$, the infalling material has a temperature gradient

$$\frac{dT}{dr} \propto \frac{d(P/\rho)}{dr} \propto \frac{d(\rho^{\gamma-1})}{dr} \propto r^{-(3/2)(\gamma-1)-1} = r^{-7/2}, \quad (\text{C9})$$

so

$$\frac{t_{\text{th}}}{t_{\text{adv}}} = \frac{3 \kappa \rho c_p \dot{M}}{224 \pi r \sigma T^4}. \quad (\text{C10})$$

This expression scales as $\rho r^{-1} T^{-3} \propto r^8$, so it is maximized at large r . Evaluating this at the Bondi radius and expanding \dot{M} with Equation (13), we find

$$\frac{t_{\text{th}}}{t_{\text{adv}}} = \frac{3 \kappa \rho_{\text{AGN}}^2 c_{s,\text{AGN}} c_p T_{\text{AGN}} \eta R_B}{224 \sigma T_{\text{AGN}}^4}. \quad (\text{C11})$$

Using $c_p T \approx c_{s,\text{AGN}}^2$ and Equation (14), we then obtain

$$\begin{aligned} \frac{t_{\text{th}}}{t_{\text{adv}}} &= \frac{3 \kappa \rho_{\text{AGN}}^2 c_{s,\text{AGN}} \eta G M_*}{112 \sigma T_{\text{AGN}}^4} \\ &= 6 \times 10^{-11} \eta \left(\frac{\kappa}{10^{-3} \text{ cm}^2 \text{ g}^{-1}} \right) \left(\frac{M_*}{M_\odot} \right) \\ &\quad \times \left(\frac{T_{\text{AGN}}}{10^3 \text{ K}} \right)^{-4} \left(\frac{c_{s,\text{AGN}}}{10^6 \text{ cm s}^{-1}} \right) \left(\frac{\rho_{\text{AGN}}}{10^{-15} \text{ g cm}^{-3}} \right)^2. \end{aligned} \quad (\text{C12})$$

Because this is extremely small, the thermal time is much shorter than the advection time for most choices of parameters.

Appendix D Accretion Stream Assumptions

We now examine the assumptions we made in determining the properties of the accretion stream. Our aim is not to ensure that every assumption is exactly upheld, but rather to see whether, if they fail to hold, that makes an order-of-magnitude or scaling difference to our results.

We begin with spherical symmetry and the steady-state assumption. Both of these assumptions are almost certainly wrong: the accretion stream is neither spherically symmetric nor time independent. Rather there will be regions that are overdense and underdense, or moving faster or slower, and which regions these are may vary with time.

We have attempted to incorporate these effects qualitatively in our treatments of mass loss and gain, because there the structure of the inflows and outflows likely matters and there are clear geometric effects, such as that an inflow and outflow cannot occupy the same space.

For the boundary conditions on temperature and pressure, we believe these assumptions matter much less. For temperature fluctuations, this is because changes on a scale less than a thermal time of the accretion stream do not alter the structure of the star or its nuclear burning. This is because the fluctuation

time for the stream is on the order of the freefall time from R_B to R_* , which is short compared with the thermal timescale for most of the star. For pressure fluctuations, we already incorporated the effects of fluctuations in Section 4.4 as an overall enhancement in mixing, as the main effect of these is to produce waves and flows that may mix the star. The same is true of aspherical temperature and pressure perturbations: these mostly serve to induce mixing (e.g., Eddington 1925) and typically become less important the farther one looks in the star (Jermyn 2015, Chapters 3, 7).

We next turn to the question of pressure support. Because the velocity scales as $r^{-1/2}$ and the density as $r^{-3/2}$, the ram pressure scales as $r^{-5/2}$. By contrast, the gas pressure scales as $\rho T \propto r^{-17/8}$, which is a weaker scaling than the ram pressure. As a result, if the ram pressure dominates over the gas pressures at any radius, it dominates everywhere inside that radius. With Equation (14) and the relation

$$P = \gamma^{-1} \rho c_s^2, \quad (D1)$$

we find

$$P_{\text{agn,gas}} \leq P_{\text{agn}} = \frac{2GM_*\rho}{\gamma R_B}, \quad (D2)$$

where γ is the adiabatic exponent. Comparing this to the ram pressure using Equation (24), we find that the gas pressure is at most on the order of the ram pressure at the Bondi radius, and the ram pressure rapidly comes to dominate farther inward.

The radiation pressure follows a similar relation. With

$$P_{\text{rad}} = \frac{1}{3} a T^4 \quad (D3)$$

and Equation (27), we find

$$P_{\text{rad}} \propto r^{-5/2}, \quad (D4)$$

which is the same scaling as the ram pressure. Hence, either the ram pressure dominates over radiation pressure at all radii or else the reverse holds. We can therefore evaluate which one dominates at the stellar radius, giving

$$\frac{P_{\text{rad}}}{P_{\text{ram}}} = \frac{a T_*^4 R_*}{3 \rho_* G M_*}. \quad (D5)$$

Using Equation (27), we have

$$\partial_r T^4 = -\frac{5T^4}{2r}, \quad (D6)$$

so we can write T^4 in terms of the luminosity and obtain

$$\frac{P_{\text{rad}}}{P_{\text{ram}}} \approx \frac{a \kappa L}{160 \pi \sigma G M_*}, \quad (D7)$$

where L here is the luminosity in the accretion stream. With $a = 4\sigma/c$ and Equation (15), we find

$$\frac{P_{\text{rad}}}{P_{\text{ram}}} \approx \frac{L}{10 L_{\text{Edd}}}. \quad (D8)$$

Hence, radiation pressure is comparable to the ram pressure only when L is large compared with L_{Edd} . This does occur in our models, likely driving super-Eddington outflows, so it is cause for some caution and further study. Nonetheless, we suspect that the order of magnitude of the boundary conditions is not substantially altered by this. This is partly because we

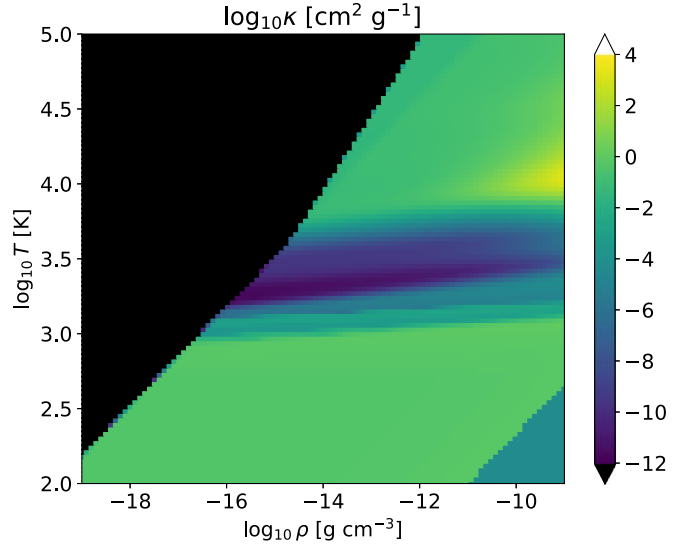


Figure 16. The opacity for a mixture of 76% hydrogen, 22% helium, and 2% solar-distributed metals is shown as a function of temperature and density.

expect aspherical effects where radiation is concentrated in some regions and attenuated in others, so it seems likely that some material is accreted at a velocity comparable to that in Equation (24), even if at other longitudes and latitudes material is flowing out at v_{esc} .

The remaining assumptions can be verified with order-of-magnitude estimates. We have claimed that the luminosity within the stream is constant. To verify this, we begin with the first law of thermodynamics in the form

$$Td s = dE + PdV, \quad (D9)$$

where E is the total specific energy including kinetic and potential and V is the specific volume. With the ideal gas law, we can write

$$PdV = -\frac{P}{\rho} d \ln \rho = -\frac{c_s^2}{\gamma} d \ln \rho. \quad (D10)$$

Assuming the stream is not pressure supported, potential energy just turns into kinetic energy and

$$dE = c_p dT \approx c_s^2 d \ln T. \quad (D11)$$

Because ρ varies more rapidly than T , we see that $|PdV| \gg |dE|$, so

$$\frac{dL}{dm} = -T \frac{ds}{dt} \approx -P \frac{dV}{dt} = \frac{c_s^2}{\gamma} \frac{d \ln \rho}{dt}. \quad (D12)$$

To integrate this through the stream, we note that

$$\begin{aligned} \int c_s^2 \frac{d \ln \rho}{dt} dm &= \int \frac{dr}{dt} c_s^2 \frac{dm}{dr} \frac{d \ln \rho}{dm} dm \\ &= \int 4\pi r^2 \rho v \frac{-3c_s^2}{2r} dr = \dot{M}_{B,\Gamma} \int \frac{-3c_s^2}{2r} dr \\ &\propto \int r^{-1} T dr \propto \int r^{-13/8} dr. \end{aligned} \quad (D13)$$

With this we obtain

$$\Delta L \approx \dot{M}_{B,\Gamma} c_{s,\text{AGN}}^2 \left(\frac{R_B}{R_*} \right)^{5/8}. \quad (\text{D14})$$

This is less than the luminosity jump at the shock, which is given by Equation (28):

$$L_{\text{shock}} \approx \dot{M}_{B,\Gamma} v^2 \approx \dot{M}_{c_{s,\text{AGN}}}^2 \frac{R_B}{R_*}. \quad (\text{D15})$$

As the luminosity in the stream is given by the intrinsic luminosity of the star plus that of the shock, so long as $L_* > 0$ the luminosity before the shock changes by at most order unity.

To show that the mass of the stream is small compared with the mass of the star, note that the mass of the stream is given by

$$M_{\text{stream}} = \dot{M}_{B,\Gamma} t_{\text{ff}} < \dot{M}_{B,\Gamma} t_{\text{ff}}, \quad (\text{D16})$$

where t_{ff} is the freefall time from R_B to R_* . This time is of order $\sqrt{R_B^3/GM_*}$, so using Equation (13) we find

$$M_{\text{stream}} < \sqrt{\frac{16\pi^2 R_B^7 \rho_{\text{AGN}}^2 c_{s,\text{AGN}}^2}{GM_*}} \approx R_B^3 \rho_{\text{AGN}}. \quad (\text{D17})$$

Even with generous values of $R_B \approx 10^{15} \text{ cm}$ and $\rho_{\text{AGN}} \approx 10^{-15} \text{ g cm}^{-3}$, $M_{\text{stream}} < 10^{-3} M_\odot$ and so is negligible compared with the mass of the star.

We have also assumed that the opacity of the accretion stream is a constant in space, though it may evolve in time. This is not true (see Figure 16), but for our purposes it suffices to be able to define an average value in the stream and have this not vary too strongly as the star evolves. Because we are concerned with an average over the stream, this may not be so bad an approximation, as the averaging process smooths over strong bumps and ridges in the opacity function. On the other hand, stellar evolution produces systematic trends in the temperature and density structure of the accretion stream, which in turn could translate into systematic trends in the mean opacity. As such, this assumption should be treated with significant caution.

Appendix E

Model Grids with Different AGN Sound Speeds

Here we show model grids for two different assumptions of the AGN sound speed, $c_{s,\text{AGN}} = 3 \text{ km s}^{-1}$ (Figures 17 and 18) and $c_{s,\text{AGN}} = 100 \text{ km s}^{-1}$ (Figures 19 and 20).

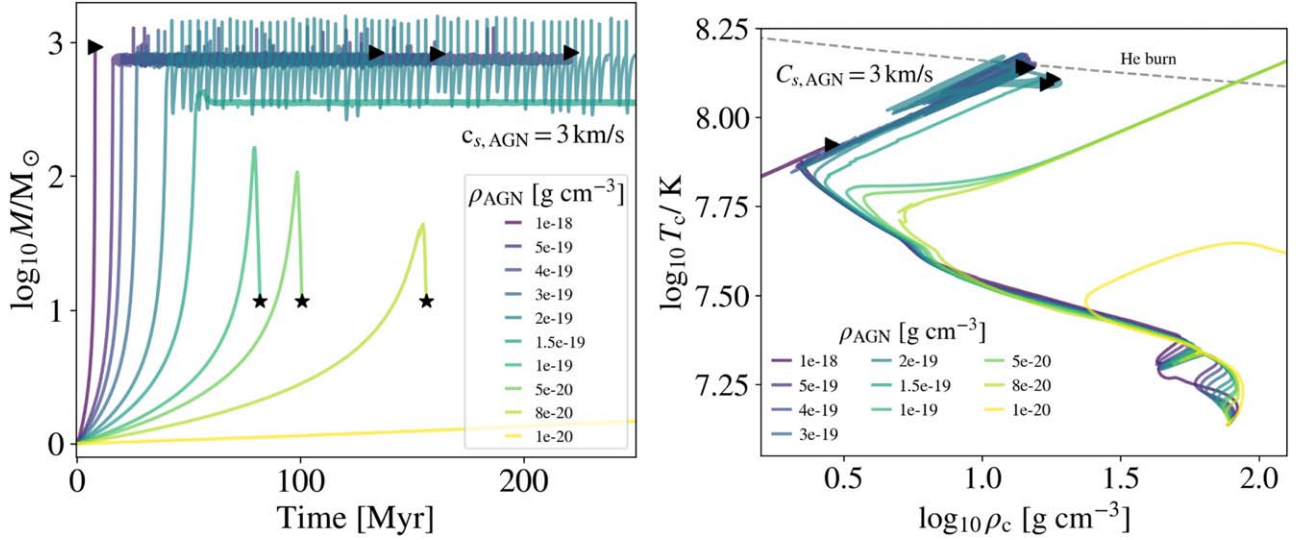


Figure 17. Grid of stellar models evolved with a fixed AGN sound speed of 3 km s^{-1} and AGN densities ranging from 10^{-18} to $10^{-20} \text{ g cm}^{-3}$. The left panel shows the evolution of stellar mass as a function of time. Models evolving at densities higher than $\approx 10^{-19} \text{ g cm}^{-3}$ experience runaway accretion and become supermassive stars (tracks ending with triangle symbols). Models evolving at densities $10^{-19} \leq \rho_{\text{AGN}} \leq 8 \times 10^{-20}$ become massive stars before losing mass via super-Eddington winds and ending their lives with $M \approx 10 M_\odot$ (tracks ending with a star symbol). At densities lower than $\approx 8 \times 10^{-20} \text{ g cm}^{-3}$, stars end their main-sequence evolution before accreting sufficient material to become massive stars ($M \lesssim 8 M_\odot$, tracks ending with a circle). The right panel shows a zoom-in of a central density–central temperature plot. Ending symbols are the same in the two panels.

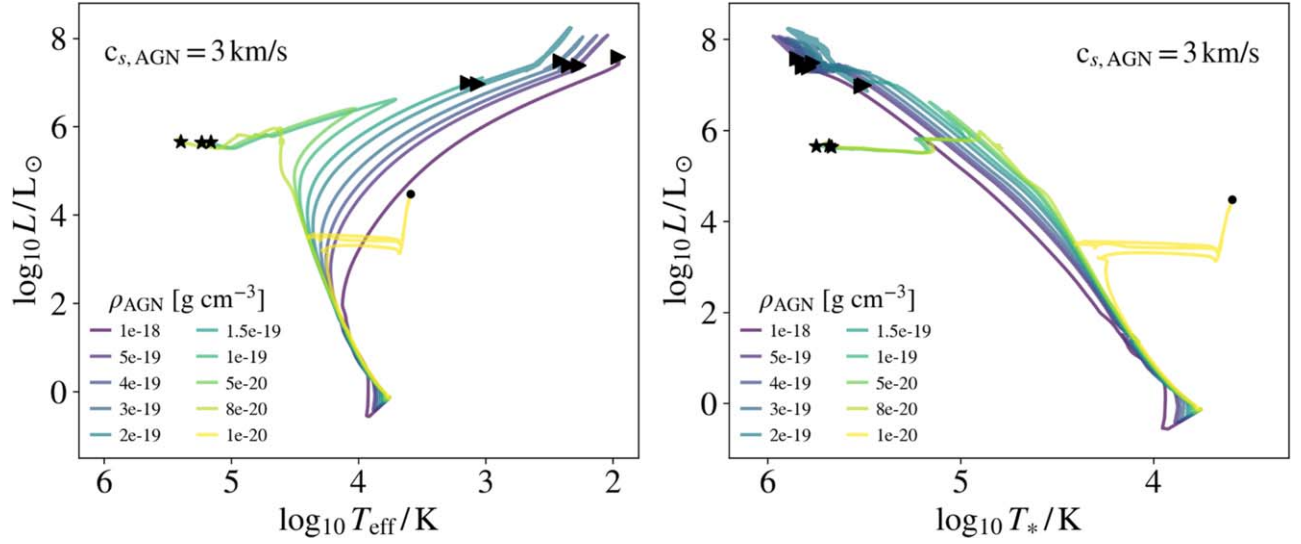


Figure 18. Evolution on the Hertzsprung–Russell diagram for the models shown in Figure 17. Left panel: the effective temperature of the models is calculated assuming electron-scattering opacity for the accretion stream. This is the temperature of the star for an observer sitting at the Bondi radius. Right panel: same as left panel, but using the surface temperature of the MESA model instead of the effective temperature (Equation (30)). This diagram is useful in understanding the type of evolution that AGN star models are undergoing, as compared to canonical stellar evolution. Note that the ending symbols are the same in the two panels.

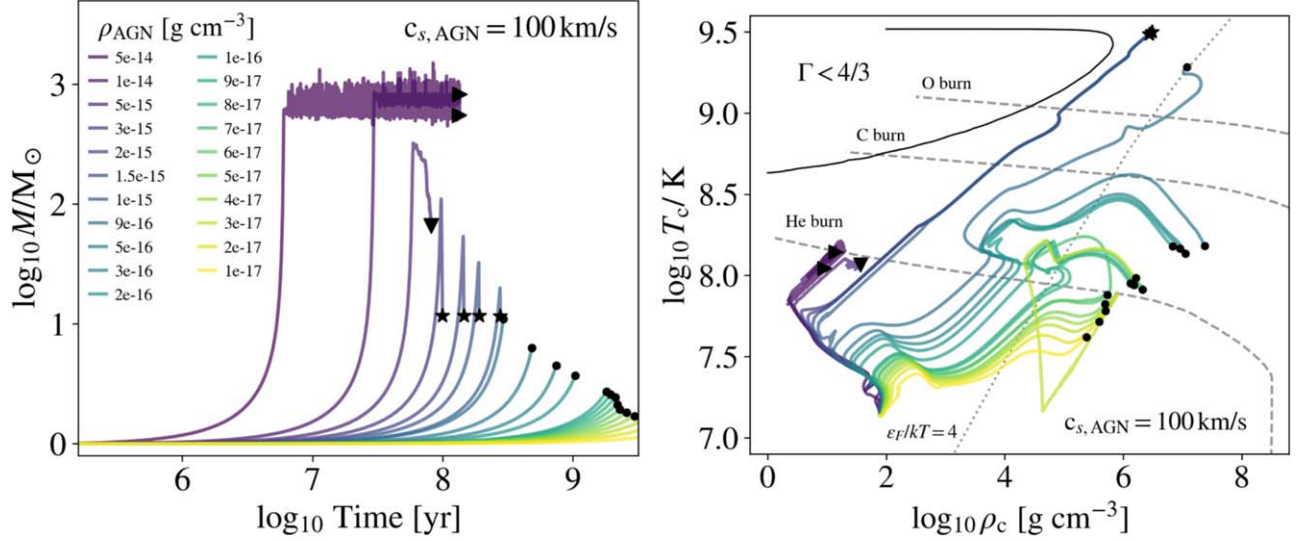


Figure 19. Grid of stellar models evolved with a fixed AGN sound speed of 100 km s^{-1} and AGN densities ranging from 5×10^{-14} to $10^{-17} \text{ g cm}^{-3}$. The left panel shows the evolution of stellar mass as a function of time. Models evolving at densities higher than $\approx 5 \times 10^{-15} \text{ g cm}^{-3}$ experience runaway accretion and become supermassive stars (tracks ending with triangle symbols). Models evolving at densities $5 \times 10^{-15} \leq \rho_{\text{AGN}} \leq 5 \times 10^{-16} \text{ g cm}^{-3}$ become massive stars before losing mass via super-Eddington winds and ending their lives with $M \approx 10 M_{\odot}$ (tracks ending with a star symbol). At densities lower than $\approx 5 \times 10^{-16} \text{ g cm}^{-3}$, stars end their main-sequence evolution before accreting sufficient material to become massive stars ($M \lesssim 8 M_{\odot}$, tracks ending with a circle). The right panel shows the evolution on a central density–central temperature plot. Ending symbols are the same in the two panels.

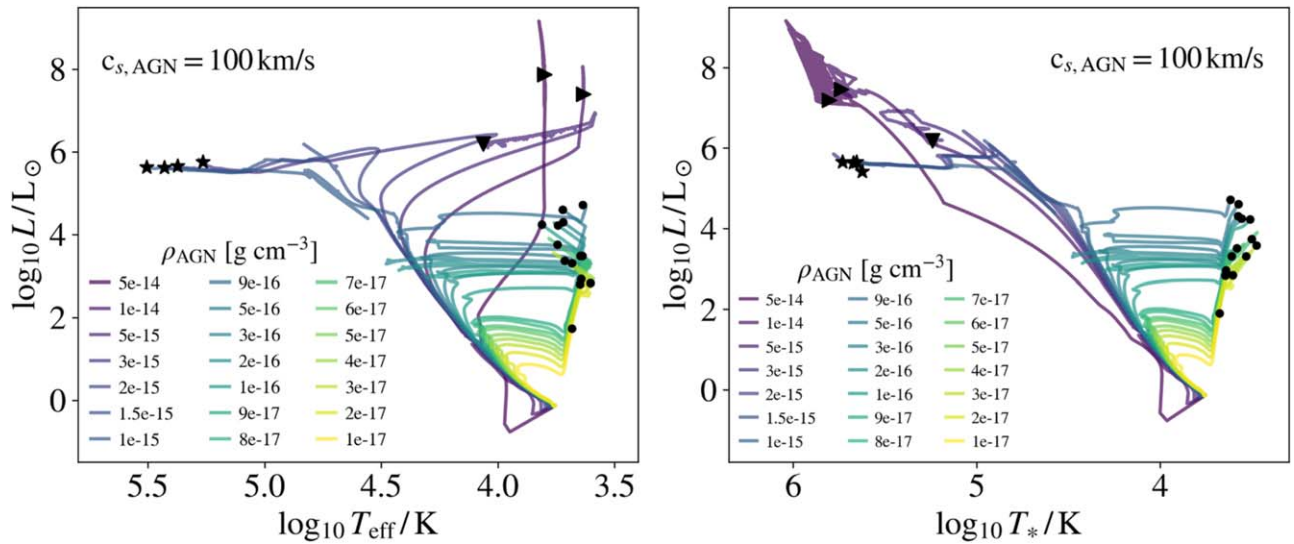


Figure 20. Same as Figure 18 but for the models shown in Figure 19.

ORCID iDs

Matteo Cantiello <https://orcid.org/0000-0002-8171-8596>
 Adam S. Jermyn <https://orcid.org/0000-0001-5048-9973>
 Douglas N. C. Lin <https://orcid.org/0000-0001-5466-4628>

References

- Abbott, R., Abbott, T. D., Abraham, S., et al. 2020a, *PhRvL*, **125**, 101102
 Abbott, R., Abbott, T. D., Abraham, S., et al. 2020b, *ApJL*, **900**, L13
 Alexander, D. M., & Hickox, R. C. 2012, *NewAR*, **56**, 93
 Alexander, R. D., Begelman, M. C., & Armitage, P. J. 2007, *ApJ*, **654**, 907
 Alexander, T. 2005, *PhR*, **419**, 65
 Alexander, T. 2017, *ARA&A*, **55**, 17
 Angulo, C., Arnould, M., Rayet, M., et al. 1999, *NuPhA*, **656**, 3
 Antonucci, R. 1993, *ARA&A*, **31**, 473
 Artymowicz, P., Lin, D. N. C., & Wampler, E. J. 1993, *ApJ*, **409**, 592
 Bahcall, J. N., & Wolf, R. A. 1976, *ApJ*, **209**, 214
 Bahcall, J. N., & Wolf, R. A. 1977, *ApJ*, **216**, 883
 Bai, X.-N., & Stone, J. M. 2011, *ApJ*, **736**, 144
 Bartko, H., Martins, F., Trippe, S., et al. 2010, *ApJ*, **708**, 834
 Bartos, I., Kocsis, B., Haiman, Z., & Márka, S. 2017, *ApJ*, **835**, 165
 Bell, K. R., & Lin, D. N. C. 1994, *ApJ*, **427**, 987
 Bellovary, J. M., Mac Low, M.-M., McKernan, B., & Ford, K. E. S. 2016, *ApJL*, **819**, L17
 Boehle, A., Ghez, A. M., Schödel, R., et al. 2016, *ApJ*, **830**, 17
 Boroson, T. A., & Green, R. F. 1992, *ApJS*, **80**, 109
 Buchholz, R. M., Schödel, R., & Eckart, A. 2009, *A&A*, **499**, 483
 Buchler, J. R., & Yueh, W. R. 1976, *ApJ*, **210**, 440
 Cassisi, S., Potekhin, A. Y., Pietrinferni, A., Catelan, M., & Salaris, M. 2007, *ApJ*, **661**, 1094
 Chugunov, A. I., Dewitt, H. E., & Yakovlev, D. G. 2007, *PhRvD*, **76**, 025028
 Collin, S., & Zahn, J.-P. 1999, *Ap&SS*, **265**, 501
 Collin, S., & Zahn, J. P. 2008, *A&A*, **477**, 419
 Cunha, K., Sellgren, K., Smith, V. V., et al. 2007, *ApJ*, **669**, 1011
 Cyburt, R. H., Amthor, A. M., Ferguson, R., et al. 2010, *ApJS*, **189**, 240
 Davies, M. B., & King, A. 2005, *ApJL*, **624**, L25
 Davies, M. B., & Lin, D. N. C. 2020, *MNRAS*, **498**, 3452
 de Mink, S. E., Sana, H., Langer, N., Izzard, R. G., & Schneider, F. R. N. 2014, *ApJ*, **782**, 7
 Dittmann, A. J., & Miller, M. C. 2020, *MNRAS*, **493**, 3732
 Do, T., Ghez, A., Morris, M., et al. 2017, in IAU Symp. 322, The Multi-Messenger Astrophysics of the Galactic Centre, ed. R. M. Crocker, S. N. Longmore, & G. V. Bicknell (Cambridge: Cambridge Univ. Press), 222
 Do, T., Ghez, A. M., Morris, M. R., et al. 2009, *ApJ*, **703**, 1323
 Do, T., Kerzendorf, W., Konopacky, Q., et al. 2018, *ApJL*, **855**, L5
 Eddington, A. S. 1925, *Obs*, **48**, 73
 Elvis, M., Wilkes, B. J., McDowell, J. C., et al. 1994, *ApJS*, **95**, 1
 Ertl, T., Woosley, S. E., Sukhbold, T., & Janka, H. T. 2020, *ApJ*, **890**, 51
 Fabian, A. C. 2012, *ARA&A*, **50**, 455
 Fabj, G., Nasim, S. S., Caban, F., et al. 2020, *MNRAS*, **499**, 2608
 Farmer, R., Fields, C. E., Petermann, I., et al. 2016, *ApJS*, **227**, 22
 Ferguson, J. W., Alexander, D. R., Allard, F., et al. 2005, *ApJ*, **623**, 585
 Ferrarese, L., & Ford, H. 2005, *SSRv*, **116**, 523
 Fragione, G., Grishin, E., Leigh, N. W. C., Perets, H. B., & Perna, R. 2019, *MNRAS*, **488**, 47
 Frank, J., King, A., & Raine, D. J. 2002, *Accretion Power in Astrophysics: Third Edition* (Cambridge: Cambridge Univ. Press)
 Fuller, G. M., Fowler, W. A., & Newman, M. J. 1985, *ApJ*, **293**, 1
 Gammie, C. F. 2001, *ApJ*, **553**, 174
 Garaud, P., & Lin, D. N. C. 2007, *ApJ*, **654**, 606
 Genzel, R., Eckart, A., Ott, T., & Eisenhauer, F. 1997, *MNRAS*, **291**, 219
 Genzel, R., Eisenhauer, F., & Gillessen, S. 2010, *RvMP*, **82**, 3121
 Genzel, R., Schödel, R., Ott, T., et al. 2003, *ApJ*, **594**, 812
 Ghez, A. M., Becklin, E., Duchjine, G., et al. 2003a, *ANS*, **324**, 527
 Ghez, A. M., Duchêne, G., Matthews, K., et al. 2003b, *ApJL*, **586**, L127
 Ghez, A. M., Klein, B. L., Morris, M., & Becklin, E. E. 1998, *ApJ*, **509**, 678
 Ghez, A. M., Salim, S., Weinberg, N. N., et al. 2008, *ApJ*, **689**, 1044
 Gillessen, S., Eisenhauer, F., Fritz, T. K., et al. 2009, *ApJL*, **707**, L114
 Goodman, J. 2003, *MNRAS*, **339**, 937
 Goodman, J., & Tan, J. C. 2004, *ApJ*, **608**, 108
 Gräfenr, G., & Hamann, W. R. 2008, *A&A*, **482**, 945
 Gräfenr, G., Vink, J. S., de Koter, A., & Langer, N. 2011, *A&A*, **535**, A56
 Graham, M. J., Djorgovski, S. G., Drake, A. J., et al. 2017, *MNRAS*, **470**, 4112
 Graham, M. J., Ford, K. E. S., McKernan, B., et al. 2020, *PhRvL*, **124**, 251102
 Gröbner, M., Ishibashi, W., Tiwari, S., Haney, M., & Jetzer, P. 2020, *A&A*, **638**, A119
 Groves, B. A., Heckman, T. M., & Kauffmann, G. 2006, *MNRAS*, **371**, 1559
 Habibi, M., Gillessen, S., Martins, F., et al. 2017, *ApJ*, **847**, 120
 Hailey, C. J., Mori, K., Bauer, F. E., et al. 2018, *Natur*, **556**, 70
 Haiman, Z., & Hui, L. 2001, *ApJ*, **547**, 27
 Hamann, F., Korista, K. T., Ferland, G. J., Warner, C., & Baldwin, J. 2002, *ApJ*, **564**, 592
 Harris, C. R., Millman, K. J., van der Walt, S. J., et al. 2020, *Natur*, **585**, 357
 Heckman, T. M., & Best, P. N. 2014, *ARA&A*, **52**, 589
 Ho, L. C. 2008, *ARA&A*, **46**, 475
 Hopkins, P. F., & Christiansen, J. L. 2013, *ApJ*, **776**, 48
 Hunter, J. D. 2007, *CSE*, **9**, 90
 Ichimaru, S. 1977, *ApJ*, **214**, 840
 Iglesias, C. A., & Rogers, F. J. 1993, *ApJ*, **412**, 752
 Iglesias, C. A., & Rogers, F. J. 1996, *ApJ*, **464**, 943
 Inayoshi, K., Ostriker, J. P., Haiman, Z., & Kuiper, R. 2018, *MNRAS*, **476**, 1412
 Ishibashi, W., & Fabian, A. C. 2012, *MNRAS*, **427**, 2998
 Ishibashi, W., & Gröbner, M. 2020, *A&A*, **639**, A108
 Itoh, N., Hayashi, H., Nishikawa, A., & Kohyama, Y. 1996, *ApJS*, **102**, 411

- Jermyn, A. S. 2015, PhD thesis, California Institute of Technology
- Jiang, J., Parker, M. L., Fabian, A. C., et al. 2018a, *MNRAS*, **477**, 3711
- Jiang, Y.-F., Cantiello, M., Bildsten, L., Quataert, E., & Blaes, O. 2015, *ApJ*, **813**, 74
- Jiang, Y.-F., Cantiello, M., Bildsten, L., et al. 2018b, *Natur*, **561**, 498
- Jiang, Y.-F., Davis, S. W., & Stone, J. M. 2016, *ApJ*, **827**, 10
- Just, A., Yurin, D., Makukov, M., et al. 2012, *ApJ*, **758**, 51
- Kennedy, G. F., Meiron, Y., Shukirgaliyev, B., et al. 2016, *MNRAS*, **460**, 240
- Khraykin, I. S., Hennawi, J. F., & Worsack, G. 2019, *MNRAS*, **484**, 3897
- King, A., & Nixon, C. 2015, *MNRAS*, **453**, L46
- Kluuyver, T., Ragan-Kelley, B., Pérez, F., et al. 2016, in *Positioning and Power in Academic Publishing: Players, Agents and Agendas*, ed. F. Loizides & B. Schmidt (Amsterdam: IOS Press), 87
- Kolykhalov, P. I., & Syunyaev, R. A. 1980, *SvAL*, **6**, 357
- Kormendy, J., & Ho, L. C. 2013, *ARA&A*, **51**, 511
- Krabbe, A., Genzel, R., Eckart, A., et al. 1995, *ApJL*, **447**, L95
- Kratter, K., & Lodato, G. 2016, *ARA&A*, **54**, 271
- Lamers, H. J. G. L. M., & Cassinelli, J. P. 1999, *Introduction to Stellar Winds* (Cambridge: Cambridge Univ Press)
- Langanke, K., & Martínez-Pinedo, G. 2000, *NuPhA*, **673**, 481
- Langer, N. 2012, *ARA&A*, **50**, 107
- Leigh, N. W. C., Geller, A. M., McKernan, B., et al. 2018, *MNRAS*, **474**, 5672
- Levin, Y. 2003, arXiv:astro-ph/0307084
- Levin, Y., & Beloborodov, A. M. 2003, *ApJL*, **590**, L33
- Li, J., Ostriker, J., & Sunyaev, R. 2013, *ApJ*, **767**, 105
- Lin, D. N. C., & Pringle, J. E. 1987, *MNRAS*, **225**, 607
- Löckmann, U., & Baumgardt, H. 2009, *MNRAS*, **394**, 1841
- Lynden-Bell, D. 1969, *Natur*, **223**, 690
- Lynden-Bell, D., & Pringle, J. E. 1974, *MNRAS*, **168**, 603
- MacLeod, M., & Lin, D. N. C. 2020, *ApJ*, **889**, 94
- Maeder, A. 1987, *A&A*, **178**, 159
- Maeder, A., & Meynet, G. 2000, *A&A*, **361**, 159
- Maiolino, R., & Mannucci, F. 2019, *A&ARv*, **27**, 3
- Mapelli, M., Hayfield, T., Mayer, L., & Wadsley, J. 2012, *ApJ*, **749**, 168
- Marconi, A., Risaliti, G., Gilli, R., et al. 2004, *MNRAS*, **351**, 169
- Martini, P., & Weinberg, D. H. 2001, *ApJ*, **547**, 12
- Martins, F., Genzel, R., Hillier, D. J., et al. 2007, *A&A*, **468**, 233
- Martins, F., Gillessen, S., Eisenhauer, F., et al. 2008, *ApJL*, **672**, L119
- McKernan, B., Ford, K. E. S., Bellovary, J., et al. 2018, *ApJ*, **866**, 66
- McKernan, B., Ford, K. E. S., Kocsis, B., Lyra, W., & Winter, L. M. 2014, *MNRAS*, **441**, 900
- McKernan, B., Ford, K. E. S., Lyra, W., & Perets, H. B. 2012, *MNRAS*, **425**, 460
- Murchikova, E. M., Phinney, E. S., Pancoast, A., & Blandford, R. D. 2019, *Natur*, **570**, 83
- Nagao, T., Marconi, A., & Maiolino, R. 2006, *A&A*, **447**, 157
- Nandra, K., George, I. M., Mushotzky, R. F., Turner, T. J., & Yaqoob, T. 1997, *ApJ*, **477**, 602
- Narayan, R., & Yi, I. 1994, *ApJL*, **428**, L13
- Nayakshin, S., & Cuadra, J. 2005, *A&A*, **437**, 437
- Nayakshin, S., Dehnen, W., Cuadra, J., & Genzel, R. 2006, *MNRAS*, **366**, 1410
- Nayakshin, S., & Sunyaev, R. 2005, *MNRAS*, **364**, L23
- Nenkova, M., Sirocky, M. M., Nikutta, R., Ivezić, Ž., & Elitzur, M. 2008, *ApJ*, **685**, 160
- Netzer, H. 2015, *ARA&A*, **53**, 365
- Neumayer, N., Seth, A., & Boeker, T. 2020, *A&ARv*, **28**, 4
- O'Connor, E., & Ott, C. D. 2011, *ApJ*, **730**, 70
- Oda, T., Hino, M., Muto, K., Takahara, M., & Sato, K. 1994, *ADNDT*, **56**, 231
- Owocki, S. P., Gayley, K. G., & Shaviv, N. J. 2004, *ApJ*, **616**, 525
- Owocki, S. P., & Shaviv, N. J. 2012, in *Instability Mass Loss near the Eddington Limit*, ed. K. Davidson & R. M. Humphreys (Berlin: Springer), 275
- Paczynski, B. 1978, *AcA*, **28**, 91
- Panamarev, T., Shukirgaliyev, B., Meiron, Y., et al. 2018, *MNRAS*, **476**, 4224
- Papaloizou, J. C., & Savonije, G. J. 1991, *MNRAS*, **248**, 353
- Paumard, T., Genzel, R., Martins, F., et al. 2006, *ApJ*, **643**, 1011
- Paxton, B., Bildsten, L., Dotter, A., et al. 2011, *ApJS*, **192**, 3
- Paxton, B., Cantiello, M., Arras, P., et al. 2013, *ApJS*, **208**, 4
- Paxton, B., Marchant, P., Schwab, J., et al. 2015, *ApJS*, **220**, 15
- Paxton, B., Schwab, J., Bauer, E. B., et al. 2018, *ApJS*, **234**, 34
- Paxton, B., Smolec, R., Schwab, J., et al. 2019, *ApJS*, **243**, 10
- Pérez, F., & Granger, B. E. 2007, *CSE*, **9**, 21
- Perna, R., Lazzati, D., & Cantiello, M. 2021, *ApJL*, **906**, L7
- Potekhin, A. Y., & Chabrier, G. 2010, *CoPP*, **50**, 82
- Pringle, J. E. 1981, *ARA&A*, **19**, 137
- Pringle, J. E., Rees, M. J., & Pacholczyk, A. G. 1973, *A&A*, **29**, 179
- Quataert, E., Fernández, R., Kasen, D., Klion, H., & Paxton, B. 2016, *MNRAS*, **458**, 1214
- Raimundo, S. I., & Fabian, A. C. 2009, *MNRAS*, **396**, 1217
- Rees, M. J., Begelman, M. C., Blandford, R. D., & Phinney, E. S. 1982, *Natur*, **295**, 17
- Roberts, S. R., Jiang, Y.-F., Wang, Q. D., & Ostriker, J. P. 2017, *MNRAS*, **466**, 1477
- Rogers, F. J., & Nayfonov, A. 2002, *ApJ*, **576**, 1064
- Saumon, D., Chabrier, G., & van Horn, H. M. 1995, *ApJS*, **99**, 713
- Schawinski, K., Koss, M., Berney, S., & Sartori, L. F. 2015, *MNRAS*, **451**, 2517
- Schmidt, M. 1963, *Natur*, **197**, 1040
- Schödel, R., Merritt, D., & Eckart, A. 2009, *A&A*, **502**, 91
- Secunda, A., Bellovary, J., Mac Low, M.-M., et al. 2019, *ApJ*, **878**, 85
- Shakura, N. I., & Sunyaev, R. A. 1973, *A&A*, **500**, 33
- Shankar, F., Weinberg, D. H., & Miralda-Escudé, J. 2009, *ApJ*, **690**, 20
- Shankar, F., Weinberg, D. H., & Miralda-Escudé, J. 2013, *MNRAS*, **428**, 421
- Shlosman, I., & Begelman, M. C. 1987, *Natur*, **329**, 810
- Sirko, E., & Goodman, J. 2003, *MNRAS*, **341**, 501
- Smith, N. 2014, *ARA&A*, **52**, 487
- Stone, N. C., Metzger, B. D., & Haiman, Z. 2017, *MNRAS*, **464**, 946
- Storchi Bergmann, T., & Pastoriza, M. G. 1989, *ApJ*, **347**, 195
- Su, M., Slatyer, T. R., & Finkbeiner, D. P. 2010, *ApJ*, **724**, 1044
- Sukhbold, T., & Woosley, S. E. 2014, *ApJ*, **783**, 10
- Syer, D., Clarke, C. J., & Rees, M. J. 1991, *MNRAS*, **250**, 505
- Tagawa, H., Haiman, Z., & Kocsis, B. 2020, *ApJ*, **898**, 25
- Tanaka, Y., Nandra, K., Fabian, A. C., et al. 1995, *Natur*, **375**, 659
- Thompson, T. A., Quataert, E., & Murray, N. 2005, *ApJ*, **630**, 167
- Timmes, F. X., & Swesty, F. D. 2000, *ApJS*, **126**, 501
- Tout, C. A., Eggleton, P. P., Fabian, A. C., & Pringle, J. E. 1989, *MNRAS*, **238**, 427
- Vink, J. S., & de Koter, A. 2005, *A&A*, **442**, 587
- Vink, J. S., de Koter, A., & Lamers, H. J. G. L. M. 2001, *A&A*, **369**, 574
- Wang, J.-M., Ge, J.-Q., Hu, C., et al. 2011, *ApJ*, **739**, 3
- Wehner, E. H., & Harris, W. E. 2006, *ApJL*, **644**, L17
- Xu, F., Bian, F., Shen, Y., et al. 2018, *MNRAS*, **480**, 345
- Yang, Y., Gayathri, V., Bartos, I., et al. 2020, *ApJL*, **901**, L34
- Yaqoob, T., Serlemitsos, P. J., Turner, T. J., George, I. M., & Nandra, K. 1996, *ApJL*, **470**, L27
- Yoon, S. C., & Langer, N. 2005, *A&A*, **443**, 643
- Yu, Q., & Tremaine, S. 2002, *MNRAS*, **335**, 965
- Zajaček, M., Araudo, A., Karas, V., Czerny, B., & Eckart, A. 2020, *ApJ*, **903**, 140
- Zhu, J.-P., Zhang, B., Yu, Y.-W., & Gao, H. 2021, *ApJL*, **906**, L11